Volume 2, Number 2 June 2020

# Nanomaterials Science & Engineering

university of aveiro tema centre for mechanical technology and automation

*Volume 2, Number 2* *June 2020*

# Nanomaterials Science & Engineering

university of aveiro tema centre for mechanical technology and automation

**Title**
Nanomaterials Science & Engineering (NMS&E), Vol.2, No.2, 2020

**Editors-in-Chief**
Igor Bdikin
Paula Alexandrina de Aguiar Pereira Marques
Duncan Paul Fagg

**Editorial Board**
Alexander Titov, Andrei Kovalevsky, António Manuel de Amaral Monteiro Ramos, António Manuel de Bastos Pereira, António Manuel Godinho Completo, Bagautdinov Bagautdin, Binay Kumar, Budhendra Singh, Cicero R. Cena, D. Pukazhselvan, Dmitry A. Kiselev, Dmitry Karpinsky, Eudes Borges de Araujo, Gil Gonçalves, Gonzalo Guillermo Otero Irurueta, Indrani Coondoo, João Paulo Davim Tavares da Silva, José Coutinho, Maciej Wojtas, Manoj Kumar Singh, Margarida Isabel Cabrita Marques Coelho, Maxim Silibin, Münir Tasdemir, Neeraj Panwar, Nikolai Sobolev, Oleksandr Tkach, Paula Celeste da Silva Ferreira, Philip Leduc, Radheshyam Rai, Sergey Bozhko, Svitlana Kopyl, Vincent Ball, Vítor António Ferreira da Costa, Vladimir Bystrov, Yuri Dekhtyar

**Editorial Managers**
Igor Bdikin
Gil Gonçalves
Raul Simões

**Cover and Logo**
Igor Bdikin (PVDF fibers microstructure, AFM image, 125x125x5 $\mu m^3$)

**Publisher**
University of Aveiro

**Support**
Serviços de Biblioteca, Informação Documental e Museologia
Centre for Mechanical Technology & Automation (TEMA)
Mechanical Engineering Department
University of Aveiro

**Copyright Information**
All work licensed under Creative Commons Attribution License that allows others to share the work with an acknowledgement of the work's authorship and initial publication in this journal. Copyrights to illustrations published in the journal remain with their current copyright holders. It is the author's responsibility to obtain permission to quote from copyright sources.

**Mailing Address**
Department of Mechanical Engineering
University of Aveiro
Aveiro 3810-193
Portugal
E-mail: bdikin@ua.pt

**ISSN:** 2184-7002

**NANOMATERIALS**
**SCIENCE & ENGINEERING**
Vol. 2, No. 2, pp. 57-73 (2020)

RESEARCH ARTICLE

https://doi.org/10.34624/nmse.v2i2.9967

---

# Graphoepitaxial growth of $CeO_2$ thin films on tilted-axes $NdGaO_3$ substrates by pulsed laser deposition

**Peter B. Mozhaev[1],*, Julia E. Mozhaeva[1], Igor K. Bdikin[2], Iosif M. Kotelyanskii[3], Valery A. Luzanov[3], Jørn Bindslev Hansen[4], Claus S. Jacobsen[4]**

*[1] Valiev Institute of Physics and Technology of Russian Academy of Sciences, Moscow, 117218, Russian Federation*
*[2] TEMA-NRD, Mechanical Engineering Department and Aveiro Institute of Nanotechnology (AIN), University of Aveiro, Aveiro, 3810-193, Portugal*
*[3] Kotelnikov Institute of Radioengineering and Electronics of Russian Academy of Sciences, Moscow, 125009, Russian Federation*
*[4] Department of Physics, Technical University of Denmark, Kongens Lyngby, DK-2800, Denmark*
**Corresponding author, e-mail address: pbmozh@gmail.com*

Received 6 December 2019; accepted 18 May 2020; published online 10 June 2020

## ABSTRACT

Growth of $CeO_2$ thin films on $NdGaO_3$ tilted-axes substrates (TAS) by pulsed laser deposition (PLD) was systematically studied in a wide range of substrate tilt angles $\gamma$ = 5-27º. The three-dimensional graphoepitaxial (3DGE) growth mechanism was demonstrated for all films on TAS. The observed deviations from the tangent 3DGE dependence can be divided into a systematic negative part and local deviations near certain film tilt angles. The systematic deviation may be explained as the effect of completely-strained coherent growth of the bottom layers of the $CeO_2$ film. The tendency of orientation of the film along the small-index crystallographic planes (012) and (013) during film growth was discovered for the first time to our knowledge. The minimization of the surface energy may account for this behavior. The width of the rocking curve and the lattice constant variation for the 3DGE $CeO_2$ films increase almost linearly with the substrate tilt angle until $\gamma$ = 19º.

At different deposition rates the 3DGE $CeO_2$ film exhibits three possible structures: (i) relaxed completely oxygenated films at very low deposition rate, (ii) completely strained well-oxygenated films at moderate deposition rates, and (iii) oxygen-deficient films consisting of two layers at high deposition rates. The deviations of orientation of the film from the 3DGE formula are set by the lattice constant c in the direction normal to the (110) plane of the substrate, which, in turn, depends on oxygen deficiency and the level of strain, introduced into the film by lattice mismatch with the substrate.

## 1. INTRODUCTION

The tilted-axes substrates (TAS)[1], also sometimes called vicinal, miscut, or offcut substrates, are single crystal substrates for epiaxial growth of thin films with a certain tilt between the substrate surface plane and the small-index crystallographic plane (SICP), providing conditions for epitaxial growth. This SICP is sometimes called "the habit plane", implying both usual formation of the film along this plane, and standard (not tilted) orientation of the crystal for substrate preparation.

---

[1] Suggested abbreviations:
TAS - tilted-axes substrate
SICP - small-index crystallographic plane
3DGE growth mechanism - three-dimensional graphoepitaxial growth mechanism
NGO - $NdGaO_3$
CMP - chemical-mechanical polishing
PLD - pulsed laser deposition
WAR-RC - rocking curve in a wide angular range
LCV - lattice constant variation

Deposition of epitaxial thin films on TAS provides unique possibilities for fine tuning of the properties of layers of anisotropic materials in planar thin film electronic devices. Application of TAS, though, have been hampered by the complexity of the film growth processes on substrates of arbitrary orientation, limiting tilt angles $\gamma$ to the vicinal range (typically $\gamma < 5^o$). Usual goal of deposition on TAS is improvement of the crystal quality of the film due to a change of the 3D growth mode (Volmer-Weber or Stranski-Krastanov) on the standard-oriented substrate to the 2D growth mode, usually the step-flow growth mode. Even this simple idea encountered a number of complications, one of which was a change of the film crystallographic orientation. The trivial assumption that the orientation of the epitaxial film follows the orientation of the habit plane is correct only for a minor part of the studied film-substrate combinations. One of the alternative growth mechanisms is the graphoepitaxial matching of the steps on the substrate surface, formed due to the faceting along the SICPs, and the height of the growth steps of the film. Such films demonstrate an inclination of their SICP from the habit plane, with an increasing tilt of the corresponding SICP of the film when the growth step of the film is higher than that of the substrate, and with a decreasing tilt from $\gamma$ when the growth step is smaller (Fig. 1). The ratio of the heights of the growth steps sets the orientational features of the film, implying essentially three-dimensional epitaxial matching between the film and the substrate, so this growth mode may be called the three-dimensional graphoepitaxial (3DGE) growth mechanism [1].

The 3DGE mechanism was first discovered in 1971 [2] and since then numerous studies reported observation of this growth mechanism in epitaxial growth of different semiconductors, metals, oxides, and in combinations of these materials (see references in [1, 3-5]). Microscopic models explaining formation of 3DGE film-substrate relations were suggested in [2-5], but usually they may be reduced to the "geometrical model", first suggested by Nagai in 1974 [6]: the initial epitaxial relation between the film and the substrate is set by lattice matching along the substrate tilt axis, while the tilt angle of the film around this axis $\gamma'$ is set by a simple formula

$$\gamma' = (c_f / c_s)\ \gamma \qquad (1)$$

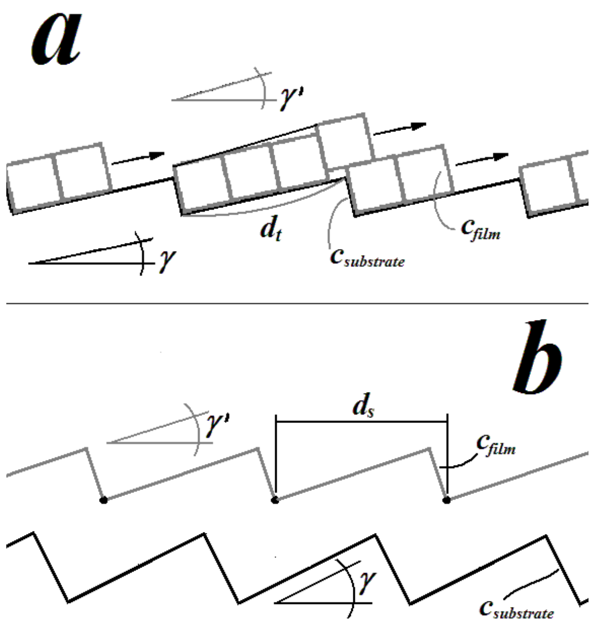

Figure 1. Simplified model of the three-dimensional graphoepitaxial (3DGE) growth of thin films on tilted-axes substrates: the inclination between the SICPs of the substrate and the film is caused by a difference between the height of the steps on the substrate surface and the growth steps of the film. The resulting tilt of the film can be higher (a) or lower (b) than the tilt of the substrate, depending on the ratio of the heights of the steps. (a) overgrowth mechanism, the tilt follows the *tangent* formula (Eq. (2) in text). (b) simultaneous seeding of the film on neighboring seeding knots (black dots) leads to the sine formula (Eq. (3)).

where $c_f$ and $c_s$ are the heights of growth steps of the film and the substrate, respectively. Extension of the "geometrical model" to the angles above 5º demands a change of the formula into

$$\gamma' = \arctan((c_f / c_s) \cdot \tan \gamma) \qquad (2)$$

or

$$\gamma' = \arcsin((c_f / c_s) \cdot \sin \gamma) \qquad (3)$$

depending on author's assumptions. Surprisingly, both variants seem to be found in different combinations of materials, with an empirical rule indicating that the *compressive* strain introduced by the SICP of the substrate into the film results in the tangent angular dependence, while the *tensile* substrate-induced strain provides 3DGE films following the sine dependence [1]. The reasons for such a difference remain unclear: the simplified models of tilt formation presented in [1] (Fig. 1a, b) do not seem convincing from any point of view. Some film-substrate combinations (namely, $CeO_2$/(110)$NdGaO_3$) demonstrated both dependences, for different deposition techniques and deposition conditions [1]. This ambiguous behavior may result from the very small lattice mismatch in the $CeO_2$ - $NdGaO_3$ combination and a very strong variation of the lattice parameter of ceria with deposition conditions, mainly oxygen partial pressure and substrate temperature.

Ceria seems to be the material which have been used to demonstrate the 3DGE growth most often of all metal oxides. A series of publications reports 3DGE growth of $CeO_2$ on $NdGaO_3$ (NGO) TAS with tilt around the [001] axis from the (110) SICP with e-beam evaporation, RF sputtering, and pulsed laser deposition (PLD) ([1, 7-9]). Deposition of $CeO_2$ on Ni tapes showed systematic 3DGE tilt of crystallites orientation in arbitrary directions [10]. Hints of 3DGE inclination of $CeO_2$ crystallites can be found in [11, 12], though the presented data are insufficient to make credible conclusions. The $\gamma' \approx 25^o$ tilt of $CeO_2$ film on a (103) $SrTiO_3$ substrate ($\gamma = 18.43^o$), as shown by the polar figures in [13], is in a good agreement with the 3DGE calculation ($\gamma' = 24.8^o$ using (2)). A tilt similar to the 3DGE growth is observed in [14], but quantitative explanation of the results demands an introduction of some interaction layer between the slopes etched in the substrate and the $CeO_2$ film, in a similar way to the $YBa_2Cu_3O_x$ 3DGE growth on the $CeO_2$ tilted-axes layers [1].

In this paper we present results of our studies of the 3DGE $CeO_2$ films on NGO TAS. The angular range $\gamma$ = 5-18º was studied in more detail compared to the previous studies, the effect of deposition conditions on orientation and properties of the 3DGE $CeO_2$ films was determined.

## 2. EXPERIMENTAL

The TAS (5×5×0.5 $mm^3$) were cut from NGO single crystals, their substrate surface was set by tilting from the (110) habit plane around the [001] axis towards the (010) plane. The nominal tilt angle was varied in the range $\gamma$ = 0 - 34º. Chemical-mechanical polishing (CMP) of the substrates provided flat surfaces with roughness $R_a$ below 2 Å, as determined by AFM. Depositions were done on the as-polished substrates, without special treatment to recrystallize the surface of the substrate, only cleaning in organic solvents and 10% HCl was performed to remove contaminants present after dicing and CMP. The actual orientation of the substrate surface after CMP was checked with XRD measurements. The deviation of the actual tilt axis from the [001] axis of NGO did not exceed 5º, usually being less than 2º.

The details of the applied PLD technique can be found elsewhere [15]. Briefly, a commercially available stoichiometric high-density (>90% of bulk density) ceramic $CeO_2$ target was used. Most of the films in this study were deposited using the process optimized for fabrication of $CeO_2$ on (1 -1 0 2) sapphire substrates: $T_D$ = 750-770 ºC, $p_{O2}$ = 0.15 mbar, $p_{total}$ = 0.5 mbar, energy density 1.5 J/$cm^2$, repetition rate 0.5 Hz [16]. This process results in rather high deposition rates, 1.2-3 Å/pulse, varying mainly with the process geometry (spot size, scan area on target, distance to substrate, etc.). In turn it demanded oxygen partial pressure $p_{O2}$ high enough (0.15 mbar) to provide complete oxygenation of the growing film, and total pressure $p_{total}$ of 0.5 mbar was necessary to suppress excessive bombardment of the growing film with energetic ions of the ablation plume. The $CeO_2$ films deposited by PLD usually grow in a mixed (001)/(111) orientation, with predominant (111) orientation when the film oxygenation is incomplete, either because of low $p_{O2}$ and insufficient deposition temperature $T_D$, or due to high deposition rate [16]. At standard deposition conditions the (111)-orientation part in $CeO_2$ films on (110) NGO substrates, determined with XRD measurements, was less than 0.1%, and typically (111) peaks could not be detected on the XRD θ/2θ-scans for thin (200-300 Å) fabricated films. The undesirable growth of (111) oriented films may be further suppressed by decreasing the deposition rate of $CeO_2$ to 0.5 Å/pulse and below. A modified deposition process with decreased energy density on target (1.1 J/cm$^2$) and lowered pressures ($p_{O2}$ = 0.012 mbar, $p_{total}$ = 0.2 mbar), resulting in a deposition rate of 0.33 Å/pulse, provided films with no signs of crystallites of (111) orientation.

No post-deposition annealing was performed; the film was cooled down to room temperature in the working atmosphere at the maximal possible rate.

The orientation and structural properties of thin films were determined using the X-ray diffraction techniques. The studies of 3DGE growth in semiconductor heterostructures showed that almost always the SICP of the film tilts around the tilt axis of TAS. To prove this behavior in $CeO_2$/NGO heterostructures we studied several samples with Laue diffraction, and found no deviations of the film tilt axis <110> from the substrate tilt axis [001]. The (001) plane of $CeO_2$ was always oriented close to the angular position of (110) NGO plane. The presence of secondary orientations was checked with rocking curves in a wide angular range (WAR-RCs), and the nature of the observed peaks was tested additionally by measurements of WAR-RC for another crystallographic plane of the film. The X-ray radiation was not monochromated or filtered with Ni filter. As a result, both sharp diffractional peaks of the broadband X-ray radiation from the SICPs of the substrate and wide diffractional peaks of

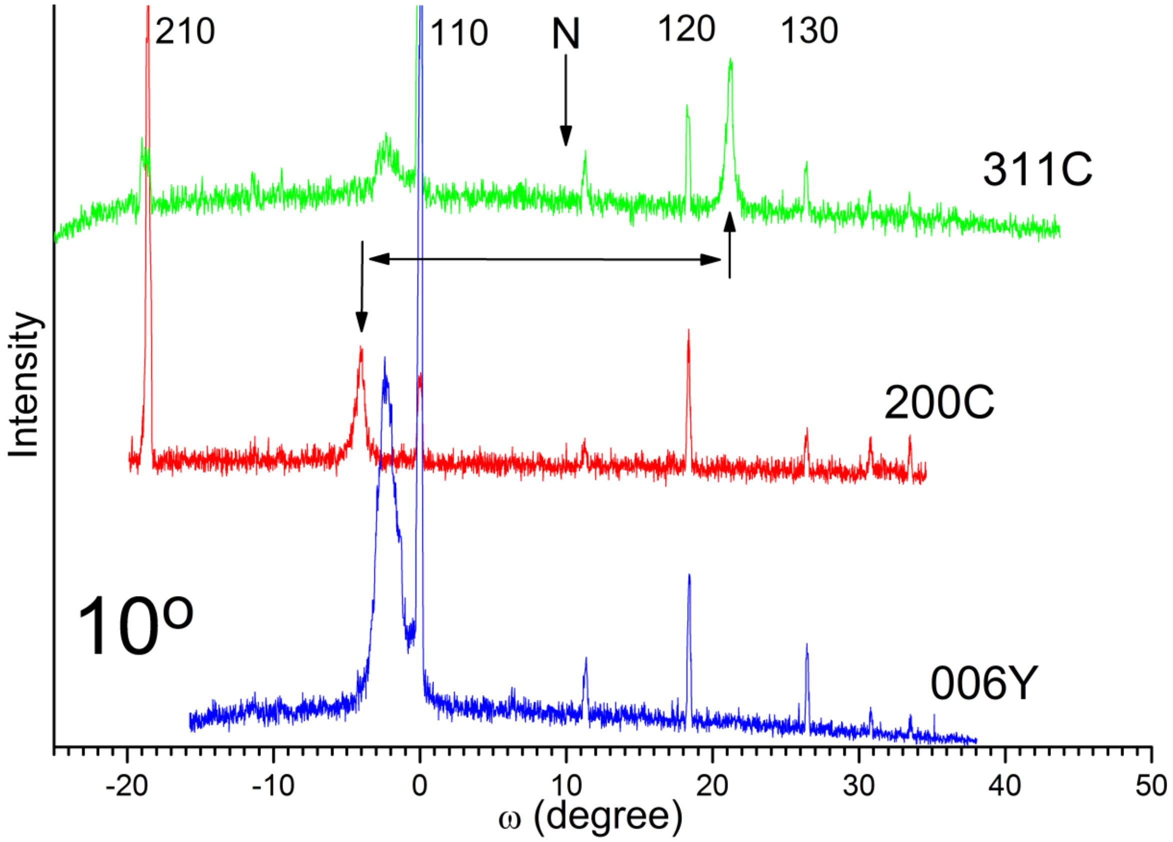

Figure 2. Determination of the orientation of 3DGE heterostructures $YBa_2Cu_3O_x/CeO_2/NdGaO_3$ with rocking curves in a wide angular range. The (110) NGO plane is tilted from the substrate plane by 10°, the position of the substrate plane is marked with "N". The broadband X-ray spectra provides peaks at the angular positions of the (210), (110), (120), and (130) SICPs of the substrate. The wide peaks from the crystallographic planes of the films are produced by the characteristic CuKα radiation at certain 2θ angular position of the detector. The additional broad peak on the top curve (ω = -3°) results from the (007) reflection of $YBa_2Cu_3O_x$ (2θ = 55°).

characteristic CuKα radiation from the SICPs of the films were observed on the same WAR-RC, providing a possibility for direct measurement of mutual inclination of the SICPs of the film and the substrate. Fig. 2 illustrates this method: a set of WAR-RCs was taken from a $YBa_2Cu_3O_x/CeO_2$/NGO heterostructure. The bottom curve corresponds to the (006) $YBa_2Cu_3Ox$ reflection (2θ = 46.5º), the medium curve to the $CeO_2$ (002) peak (2θ = 33º), and the top curve - to the (113) $CeO_2$ peak (2θ = 56.5º). The inclination of the "(311)" peak of ~26.5º from the (001) plane of $CeO_2$ proves that (i) both reflections are obtained from the same part of the film, and (ii) the in-plane orientation of $CeO_2$ corresponds to the standard epitaxial relation for fluorite growth on $NdGaO_3$: <110>(001)$CeO_2$||[001](110)NGO. No other orientations of $CeO_2$ were detected in the sample.

The deposition rate was calibrated using lift-off removal of some part of the deposited film using a mask stable at high deposition temperature. We call the *nominal thickness* the product of the number of pulses on target and the calibrated deposition rate. The thickness was also evaluated using the Williamson-Hall method, the result was in good agreement (error below 15%) with the nominal value for $CeO_2$ films on a standard (110) oriented NGO substrate. The Williamson-Hall estimations of film thicknesses for simultaneously deposited samples with different tilt angles ($\gamma$ = 0-12º) showed results within 10% variation from sample to sample, so we may conclude that the film growth rate is almost independent on the substrate tilt angle at least for small $\gamma$.

In addition to the crystallite size (thickness) value the Williamson-Hall method provides estimation of the *Δd/d* parameter, expressing weighted spread of the interplane distance *d* in the sample. For diffraction on the *(00l)* planes of the films with orientation close to (001) this parameter is reduced to the spread of the *c* lattice constant *Δc/c*. Sometimes *Δd/d* is called "strain", because for some epitaxial films a relation can be established between *Δd/d* and the elastic strain introduced into the film by the substrate. To avoid misunderstanding, we call the *lattice constant variation* (LCV) the *Δc/c* parameter, determined for diffraction on the *(00l)* $CeO_2$ planes.

The surface morphology of the films was studied with a Tencor Alfa-Step 200 profiler and a NanoSurf EasyScan AFM.

We would like to note that the main goal of fabrication of the 3DGE $CeO_2$ films was fabrication of YBCO/$CeO_2$/NGO heterostructures for the needs of another experiment (tilted-axes biepitaxial thin film structures of high-temperature superconductor YBCO, [17, 18]), so the structure and properties of the $CeO_2$ layer was not studied thoroughly for all fabricated films and multilayers. The θ/2θ-scans for some samples were taken in a narrow θ range or even were absent because of complications of measurements in the asymmetric diffraction geometry. These circumstances resulted in an ample collection of rocking curves measurements, providing tilt angle of the film and spread of the orientations of the crystallites of the film, but a rather moderate set of θ/2θ-scans, especially for the single $CeO_2$ layers before YBCO capping layer depositions. As a consequence, determination of dependences of lattice constant c and LCV is difficult and our considerations sometimes are inconclusive.

## 3. RESULTS AND DISCUSSION

As we mentioned above, all films showed strict alignment of the <110> axis of the film with the tilt axis of the substrate [001] NGO. The epitaxial relations were expressed as angular proximity of the (001) SICP of the film and the crystallographic plane of standard epitaxial growth (habit plane), (110) NGO, with inclination angle between the films set by the 3DGE growth relation (2).

To avoid misunderstanding we will use the following notation:

- the substrate plane is the plane of substrate surface;
- the tilt angles $\gamma'$, $\gamma$ are the angles between the substrate plane and the SICP of the film and the substrate, respectively;
- the inclination angle is the angle between the SICPs of the substrate and the film;
- the mis-orientation is the spread of orientations of individual crystallites of the film around the main orientation, usually determined as

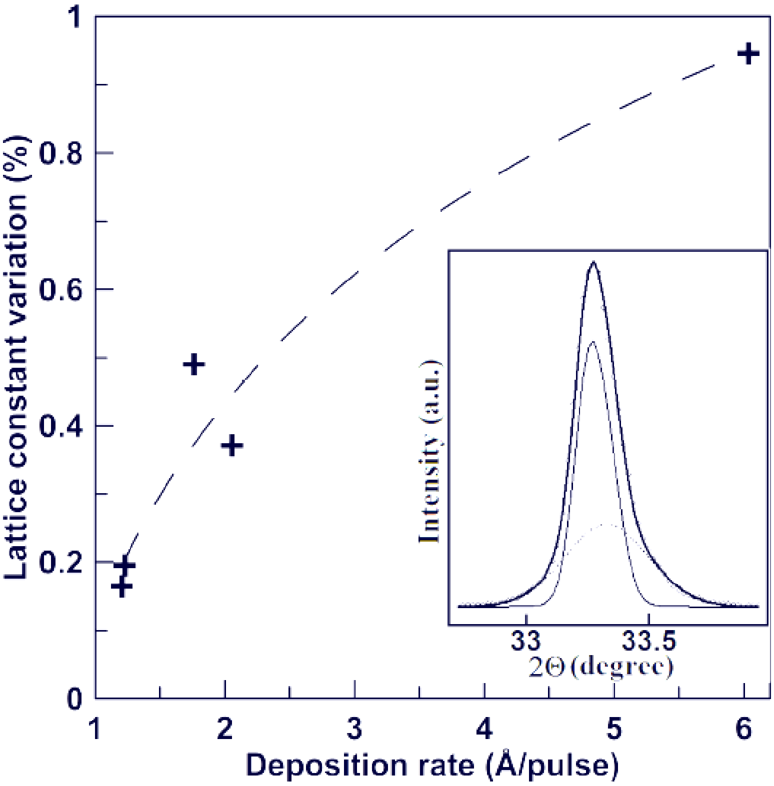

Figure 3. The lattice constant variation of $CeO_2$ films on (110) NGO substrates increases with deposition rate (the dashed line is a guide for the eye). Inset: the (002) peak of a thick $CeO_2$ film may be resolved into two peaks shifted in angular positions, implying a difference in the lattice constants for the corresponding parts of the film.

full width at half maxima (FWHM) of the corresponding rocking curve.

### 3.1. Standard epitaxial growth of $CeO_2$ films on (110) NGO substrates

$CeO_2$ films deposited with the standard process (deposition rate 1.2-1.8 Å/pulse for the chosen geometry of deposition) exhibited a lattice constant of 5.395-5.401 Å, close to the reference bulk value of 5.4 Å. The LCV is small, 0.1-0.5%, implying high in-depth homogeneity of the films. The width of the rocking curve for (002) peak (2θ = 33°) of the $CeO_2$ films on (110) NGO substrate 0.34±0.09° just slightly exceeds the FWHM of the rocking curve of the substrate (0.28±0.04° for the (440) peak at 2θ = 47°). The relatively high value of the latter results from the geometrical limitations of the measurement; at high 2θ angles (70° and more) the FWHM of the rocking curve of the substrate decreases to 0.05-0.08°, an indication of the single crystal character of the substrate. The $CeO_2$ peaks for this angular range are weak, making precise measurements of the rocking curves complicated.

An increase of deposition rate to 6 Å/pulse leads to an increase of lattice constant to 5.404 Å. The LCV of such films increases to ~1% (Fig. 3), manifesting non-uniform structure of thick films fabricated at high deposition rate. The X-ray θ/2θ-scans of the thick (~1500 Å) film deposited at high deposition rate allows decomposition of the (002), (004) peaks of ceria into two contributions: a narrow peak (corresponding lattice constant 5.409 Å, LCV 0.33%, estimated thickness 1290 Å) and a wide peak (5.404 Å, 0.62%, 360 Å), see inset in Fig. 3. The LCV of ~1%, estimated for the whole film, is higher than the LCV values for both film parts because the lattice constant values are different for the two parts of the film. The ratio of integral intensities of the narrow and wide peaks for the (002) peak is ~1.33, and ~0.56 for the (004) peak. This increasing "visibility" of the wide peak

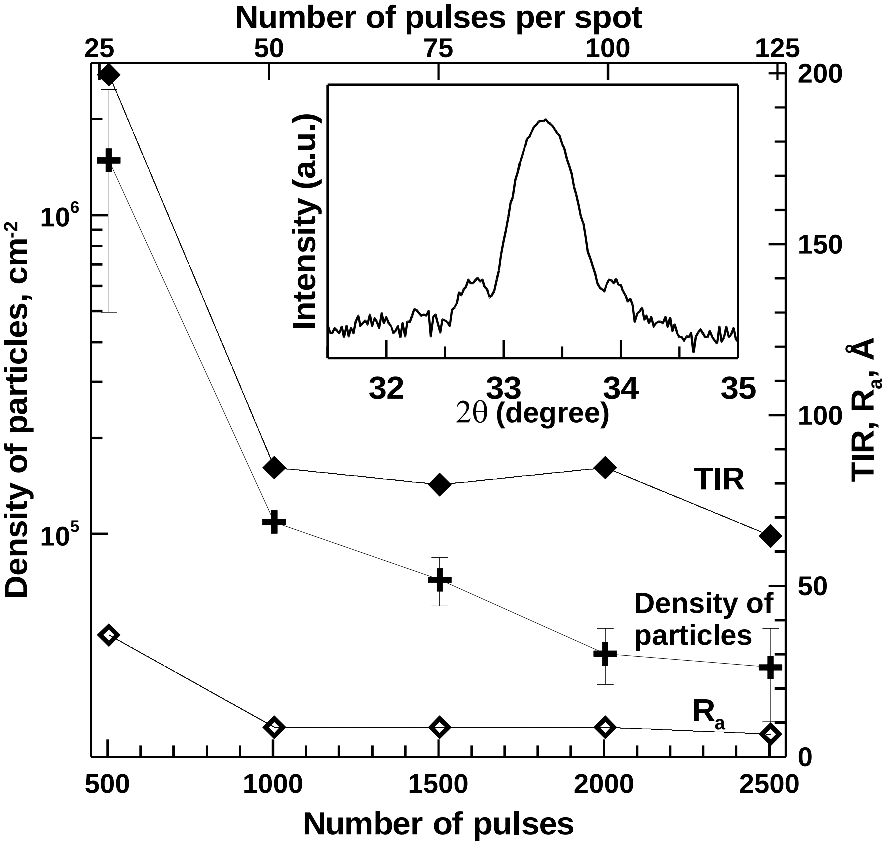

Figure 4. Evolution of parameters of $CeO_2$ film surface morphology (roughness, density of particles, and total range of the profiler measurement on a 100 nm scan) as a result of metallization of the target surface under laser irradiation. Inset: the $CeO_2$ films deposited from a ceramic target show clear Laue oscillations on the X-ray θ/2θ-scans.

for the higher measurement angle θ may be interpreted as a presence of two layers in the film, with the narrow peak corresponding to the top layer. The sum of the estimated thicknesses is close to the nominal thickness of the film, corroborating our assumption of formation of two layers. The splitting of the peaks of the θ/2θ-scans was never observed for the films grown with deposition rate of 1-2 Å/pulse, but could be detected for some of the films fabricated at 3 Å/pulse.

The observed features can be explained as the result of relaxation of the substrate-induced tensile strain. The top layer represents the relaxed part of the film over certain relaxation thickness; the value of ~350 Å is quite typical for oxide films growth. The lattice constant of the relaxed layer ~5.41 Å is higher than 5.398±0.003 Å, observed for the films deposited with low deposition rate, probably as a result of incomplete oxygenation of the film deposited at high rate. The bottom layer shows a smaller *c* value, 5.404 Å, due to the distortion generated by the substrate-induced tensile biaxial strain. Continuous relaxation of this strain with thickness, with corresponding increase of the *c* lattice constant, may be responsible for the high LCV value for the bottom layer. A relatively small distortion of the *c* lattice constant (0.2-0.5%, depending on the applied model) compared to the substrate-induced strain of ~1% implies formation of semi-coherent interface with the substrate, typical for defect fluorites.

The X-ray diffraction studies, the thickness measurements, and the AFM surface observations showed a strong dependence of properties of the $CeO_2$ films on the modification of the target surface (Fig. 4). Under laser irradiation the surface of $CeO_2$ ceramic target gains metallic glitter, probably as a result of loss of oxygen. Such metallization of the target surface significantly changes the properties of the $CeO_2$ film. The deposition rate from the ceramic target is almost 1.5 times higher than from a completely developed metallized surface. The decrease of the deposition rate is very fast and takes place after just 10-15 shots per each spot on the target. The films deposited from the ceramic target show thickness fringes (Laue oscillations) on the θ/2θ-scans (see inset in Fig. 4), manifesting high smoothness of the film surface and good homogeneity of the film. At the same time, estimation of the LCV in the films prepared from the ceramic target, exhibits rather high values even at low deposition rate, e.g., 0.5% at 1.8 Å/pulse or 0.45% at 1.2 Å/pulse (compare with data from a metallized target in Fig. 3). Simultaneous observation of thickness fringes and increased LCV may be accounted for the lattice constant inhomogeneity found in the x-y plane (along the film surface), and not along the z-direction (in the films growth direction). The excessive LCV disappears after 15-20 shots per spot on the target, but the thickness fringes are still observed up to ~25 shots per spot. After 25 shots the films never demonstrate thickness fringes (for a typical peak shape for such films see inset in Fig. 3), but the evolution of surface morphology just starts (Fig. 4). The mechanisms for smoothening of the $CeO_2$ film surface deposited from a metallized target are outside the frame of this article and will be discussed elsewhere. They were briefly considered in the discussion of yttria nanoparticle formation in Ref. [19].

All properties, both structural and morphological, of the $CeO_2$ films on (110) NGO substrates, did not change after each spot on the target was irradiated with ~150 shots. Removal of the metallized layer from the surface of the target with grinding completely restores the properties of the fabricated films. To improve reproducibility of the experiment, we decided to fabricate $CeO_2$ films

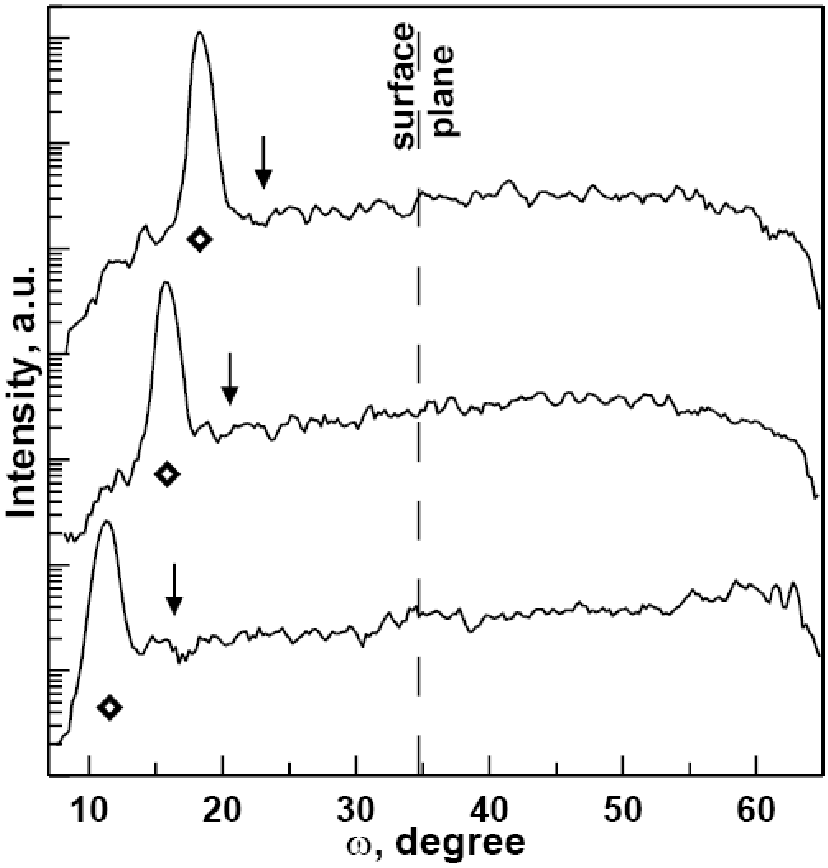

Figure 5. XRD rocking curves for the (004) $CeO_2$ peak of the 3DGE films on NGO TAS. The positions of the (110) planes of the substrates are marked with arrows, the substrate tilt angles are 11.4, 14, and 18.7°, from top to bottom. The (004) peaks of the $CeO_2$ films are marked with diamonds, the tilt angles are 16.5, 19.25 and 24.5°, in a good agreement with the geometrical model (2).

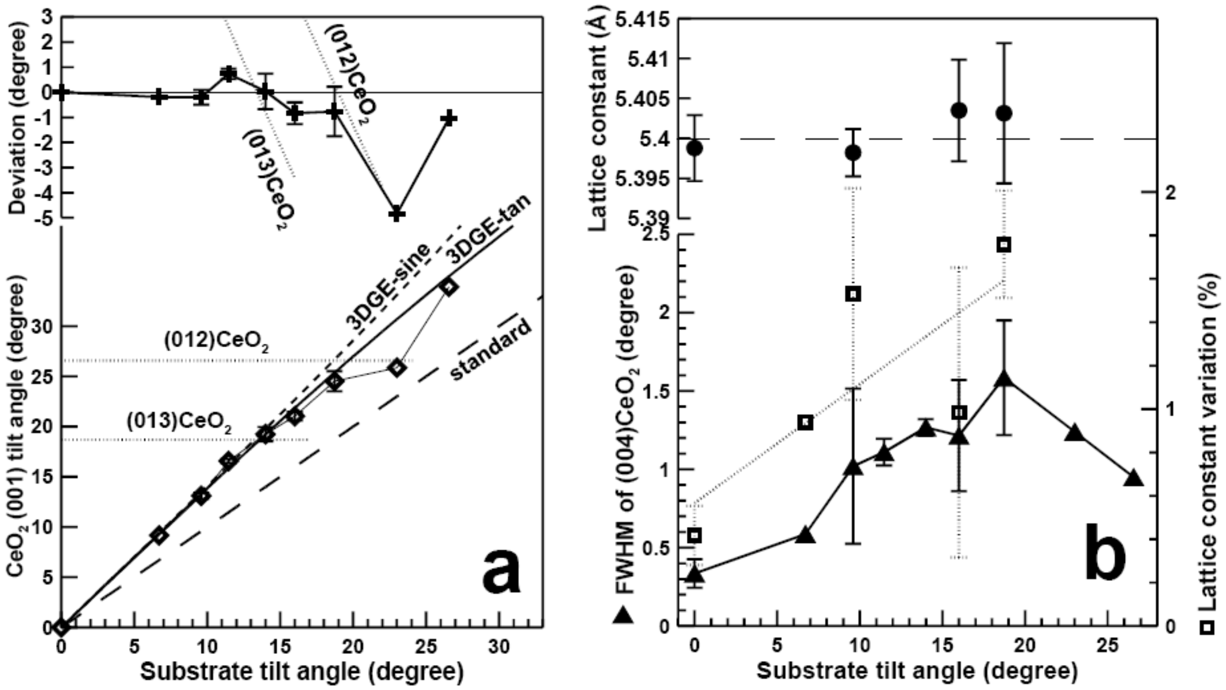

Figure 6. Angular dependences for the parameters of the 3DGE $CeO_2$ films on TAS NGO. a) the film tilt angle follows the 3DGE tangent dependence (2) with a small negative deviation. More intense deviations are observed in vicinity of the SICPs of the film, (013) and (012). b) Top: the lattice constant slightly increases with tilt angle. Bottom: the width of the rocking curve (triangles) increases until $\gamma \approx$ 20º, and decreases at higher angles. The LCV (squares) increases in the range 0-20º. The error bars here and on all subsequent figures are representing the spread of measured parameters of $CeO_2$ films.

only from a saturated metallized target, sacrificing the improved structural perfection of the films deposited from a ceramic target. Our main reason was that we have been unable to distinguish the effects of thickness and the effects of target metallization on the film properties when a ceramic target is ablated.

Summarizing, the $CeO_2$ films fabricated with our standard process showed good crystallinity and small mis-orientation of crystallites. An increase of deposition rate above 2 Å/pulse results in an incomplete oxygenation of the films for the chosen $p_{O2}$ = 0.15 mbar, with development of non-uniform film as a result of relaxation of the substrate-induced strain with thickness. The metallization of the target surface complicates interpretation of the obtained results, so further depositions were performed from the saturated metallized target to avoid incontrollable changes in the deposited material.

### 3.2. 3DGE growth of CeO₂ films on TAS NGO

The typical rocking curves of the $CeO_2$ films deposited by PLD on TAS NGO are presented on Fig. 5. The (004) $CeO_2$ peak is shifted from the position of the (110) NGO plane towards higher tilt angles, in an agreement with the higher growth step of the $CeO_2$ film compared to the steps on the substrate surface (5.4 and 3.864 Å, respectively). The shift increases with the substrate tilt angle, confirming the 3DGE growth mode. A better fit of the experimental data is provided by the tangent dependence, Eq. (2).

An increase of the tilt angle $\gamma$ above 30º results in an increase of the film tilt angle $\gamma'$ to 45º and growth of (110)-oriented $CeO_2$ films for all tilt angles from 30 to 45º. The properties of the (110) $CeO_2$ films for the tilt angles from 30 to 45º will be presented elsewhere.

#### *3.2.1. Angular dependences*

The general dependences of the parameters of the $CeO_2$ 3DGE films on the substrate tilt angle are shown on Fig. 6. The orientation of all samples with varying thickness and deposited under different deposition conditions are following the same 3DGE relation (Fig. 6a). The agreement with the calculated value is good, a small systematic deviation to the smaller tilt angles may be pointed out (Fig. 6a, top). More significant deviations are observed in the vicinity of $\gamma$ = 12º (positive deviation, film tilt angle $\gamma'$ ≈ 17º) and $\gamma$ = 23º (strong negative deviation, film tilt angle $\gamma'$ ≈ 26º). One of possible explanations is a tendency to minimization of surface energy when the surface plane of the film aligns with a SICP. The positions of (013) ($\gamma'$ ≈ 18.43º) and (012) ($\gamma'$ ≈ 26.57º) planes are shown with dotted lines on Fig. 6a: the experimentally observed deviations are clearly attracted towards these lines. The higher intensity of the deviation at 23º may be due to a smaller sum of indexes of the (012) plane, indicating a more pronounced minimum of surface energy compared to the (013) plane.

The angular dependences of the main features of the $CeO_2$ 3DGE films are presented on Fig. 6b. The width of the rocking curve shows a linear rise with the tilt angle until ~19º, and then a linear decrease. The lattice constant variation repeats this dependence over the range where LCV estimation was possible. Note that LCV shows a very high spread of estimated values due to the application of diverse processes with deposition rate ranging in a wide interval.

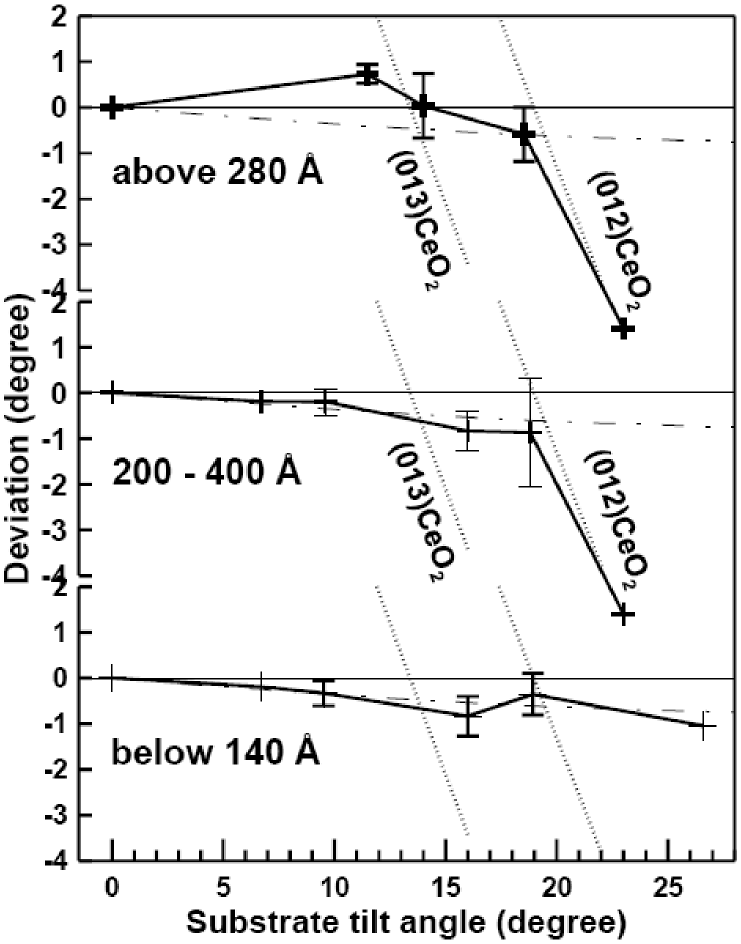

Figure 7. Evolution of the angular dependence of the deviation of the film orientation from the calculated 3DGE value. Thin films (bottom graph) follow the 3DGE tangent dependence (2) with a smaller lattice constant of the film, the corresponding calculated deviation is presented with a dash-dotted line. The films with medium thickness (middle graph) show deviation towards (012) $CeO_2$ orientation at substrate tilt angle of 23º. Finally, thick films (top graph) show clear deviations towards (013) and (012) $CeO_2$ orientations.

The lattice constant of the 3DGE $CeO_2$ films did not change much with the tilt angle (see Fig. 6b, top graph). The average value slightly increased for higher LCV and FWHM of the rocking curve, revealing less homogeneous films with higher density of defects in the 15-20º angular range. Usually the dominant type of defects in $CeO_2$ are oxygen vacancies, and an increase of their density results in an expansion of the lattice with a consequent increase of the lattice constant.

The complicated features of the general dependence of the deviation from the calculated value (Fig. 6a, top curve) may be resolved when the particular angular dependences for films of different thicknesses are presented independently (Fig. 7). The thin films show a smooth dependence with a small negative deviation increasing with the tilt angle. For the film tilt dependence on the substrate tilt angle (Fig. 6a, bottom) this would correspond to a tangent dependence (2) with a reduced film step height $c_f$. Such shrinking of the out-of-plane lattice constant of the growing film may result from a substrate-induced biaxial tensile strain; indeed, the NGO substrate with lattice constant of 3.864 Å (assuming pseudo-cubic lattice) introduces a tensile biaxial strain of ~1.3% into the growing $CeO_2$ (assuming completely oxygenated $CeO_2$ with lattice constant of 5.395 Å and taking into account the 45º in-plane tilt of $CeO_2$ axis from the <100> axes of the substrate). This strain, in the volume-preserving approximation (Poisson ratio $\nu$ = 0.5), produces a shrinking of the out-of-plane lattice constant to 5.258 Å. We have calculated the expected deviation from Eq. (2) assuming a decrease of the step height to the estimated value, and obtained an excellent agreement with the observed negative deviation of the orientation of the thin $CeO_2$ films from the values calculated for the saturated lattice constant (Fig. 7, dash-dotted lines). We may conclude that most probably (i) the film is seeded completely coherently strained along the (110) NGO plane, (ii) the film is completely oxygenated during seeding, the relaxed lattice constant $c_{relax} \approx 5.395$ Å, (iii) the orientation of the seed follows the tangent formula (2) exactly, and (iv) the volume of the unit cell of a completely oxygenated ceria is preserved under biaxial distortions, $\nu$ = 0.5. The latter is not the case for oxygen-deficient ceria, the usual Poisson ratio for the $CeO_2$ films containing oxygen vacancies is about 0.3.

An increase of the film thickness results in deviations from the initial orientation (shown as dash-dotted lines in Fig. 7). Already at ~300 Å the film on the 23º-tilted substrate turns towards the (012) $CeO_2$ orientation (Fig. 7, middle graph), but the overall dependence still follows the initial orientation set by the strained bottom layers of the film. Further increase of thickness results in a pronounced deviation also at film tilt of ~18.5º, corresponding to the (013) $CeO_2$ SICP orientation (Fig. 7, top graph).

To be fair, we must point out that we have fabricated only one sample at $\gamma$ = 23º and one sample at 26.5º, so any conclusion on the angular dependences in this range is not well founded. As a consequence, a completely reliable result is presented only on the bottom graph of Fig. 7.

### *3.2.2. Effect of deposition rate and thickness on the properties of the 3DGE CeO₂ films*

An important drawback of our study is the fact that we are not able to distinguish reliably the effect of thickness and the effect of deposition rate: a significant part of the fabricated samples differed in thickness due to the changes of the geometry of deposition, and, hence, the deposition rate.

The effect of deposition rate can be illustrated by Fig. 8. An increase of deposition rate can lead to incomplete oxygenation of the growing film, with corresponding increase of the measured $c$ lattice constant. In our deposition system with $p_{O2}$ = 0.15 mbar during the standard deposition process, complete oxygenation (lattice constant 5.395-5.397 Å) may be obtained for deposition rates below 2 Å/pulse (Fig. 8). The deposition rate of 3 Å/pulse is slightly excessive and results in a broad variation of lattice constants depending on the repetition rate (in fact, the period between the pulses), the substrate tilt angle, the film thickness, etc. The observed dependence is in an excellent agreement with our results on standard (110) NGO substrates, see Section 3.1.

The common effect of pressure and deposition rate is demonstrated by the dependence of lattice constant on the oxygen partial pressure at a relatively low deposition rate of 1 Å/pulse (see inset in Fig. 8). A decrease of oxygen partial pressure

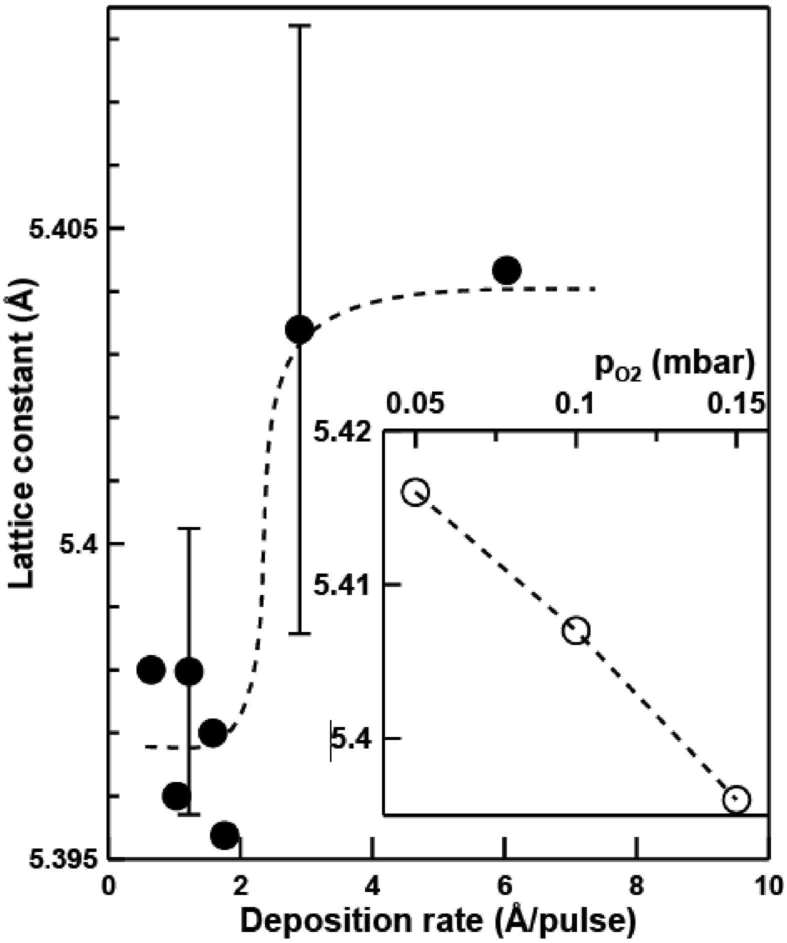

Figure 8. Lattice constant dependence on deposition rate for the 3DGE $CeO_2$ films, oxygen partial pressure 0.15 mbar. Inset: lattice constant dependence on oxygen partial pressure, deposition rate 1 Å/pulse.

results in a monotonous increase of the lattice constant up to 5.416 Å at $p_{O2}$ = 0.05 mbar, implying that insufficient oxygenation is the main reason for the expansion of the c lattice constant with an increase of the deposition rate at constant $p_{O2}$.

The effect of thickness on the properties of the 3DGE $CeO_2$ films can be clarified if the samples are divided according to the deposition rates, below 2 Å/pulse and above. The data for the tilt angle 18.43° are presented in Fig. 9, the open symbols of all the graphs of Fig. 9 correspond to low deposition rate samples, while closed symbols show the features of the films grown at high deposition rate. Considering the presented results please keep in mind that we could not completely remove the dependence on deposition rate from the thickness dependences, because the thinner films were generally obtained at lower deposition rates than the more thick ones.

The deviation from the calculated film tilt value (using the standard 5.398 Å step height) for the low-rate films is small, <1° (Fig. 9a). Excluding the point at 40 Å with extremely low average deposition rate (0.4 Å/pulse × 0.1 Hz = 0.04 Å/s), we get the deviation from the calculated value almost independent on thickness and close to the value for the coherently strained ceria (-0.6°, the dash-dotted line on Fig. 9a). Taking into account the influence of deposition rate on the observed thickness dependence, we may suppose that the strain introduced into the film by lattice mismatch increases with deposition rate (revealed by an increase of thickness). This is in a good agreement with our observations for the $CeO_2$ films on (110) NGO substrates: the lattice constant c for slowly

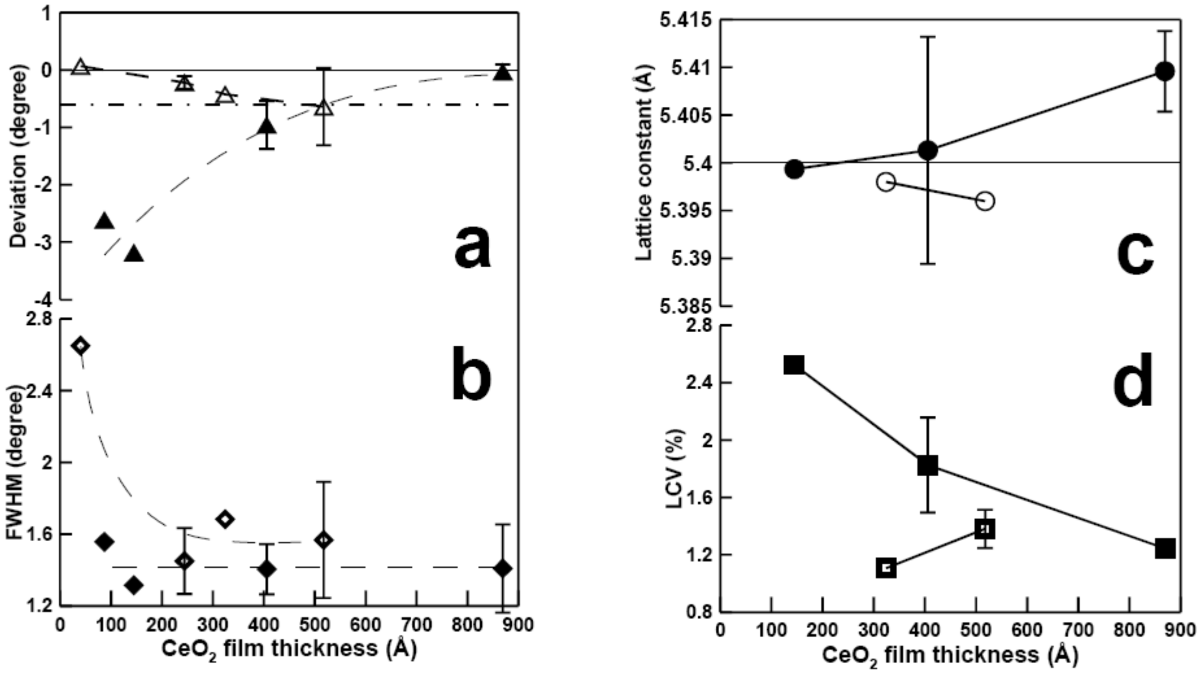

Figure 9. Thickness dependences of properties of the 3DGE $CeO_2$ films deposited at different deposition rates, substrate tilt angle 18.43º. Open symbols on all graphs correspond to deposition rates 1.5 Å/pulse and below, closed symbols - to deposition rates 2.5 Å/pulse and above. The lines are given as guides for the eye.

grown films is close to the standard value and the LCV is very small, down to 0.1%. These observations imply very low or negligible effect of substrate misfit, in a contrast with the films grown at high rates, with clear lattice constant contraction and relaxation of the introduced distortion with thickness. The weak bonding over the film-substrate interface at a very low deposition rate is corroborated by a very high width of the rocking curve for the film grown at the extremely low rate (Fig. 9b). All other low-rate films showed very close values of FWHM, ~1.6º (Fig. 9b). The lattice constant is small, 5.396-5.398 Å, again in a good agreement with the data on the $CeO_2$ films deposited on standard (110) NGO substrates at low deposition rates (Fig. 9c). The LCV, though, is significantly higher, ~1.3% (Fig. 9d), the reasons for this should be clarified additionally.

Summarizing, the 3DGE $CeO_2$ films deposited at low deposition rate strongly resemble the $CeO_2$ films grown on standard (110) NGO substrates at low rate: they are fully oxidized, with low level of substrate-induced strain. The orientation of the films is set by the contracted c due to the substrate-induced strain, but the introduced strain is decreased with lowering the deposition rate. High density of oxygen vacancies of the substrate surface during seeding may promote substrate-film bonding, explaining the observed influence of deposition rate on the level of substrate-induced strain. Another good explanation of the observed orientational behavior of the films grown at low deposition rate is enhanced relaxation at very low deposition rates. If this supposition is correct, then the relaxation periods between the laser pulses at the extremely low deposition rate is high enough to completely remove all substrate-induced strain for the first unit-cell-thick layers of the $CeO_2$ films, as the orientation of the film exactly corresponds to the calculated using the lattice constant of a relaxed $CeO_2$ film.

The behavior of the films deposited at high deposition rate is more complicated. An increase of thickness (keeping in mind the corresponding increase of deposition rate, at least for some films of the set) leads to an increase of the lattice constant (Fig. 9c), in a very good agreement with the data for the films on standard NGO substrates:

thin films show *c* =5.4 Å, but for thick films it increases to 5.41 Å. An increase of *c* with thickness is monotonous from the most thin films studied, and can be attributed to the relaxation of the substrate-induced strain with thickness. The thickness of 350-400 Å sets the border between thin and thick films (see the increased slope of the c dependence on thickness, Fig. 9c), and the high spread of the measured *c* value for this range may be referred to changing critical thickness with a deviation of the deposition parameters. The LCV dependence generally supports these considerations: the most intense change of the c lattice constant is expected for the thin films as a result of strain relaxation, and the LCV, in fact, shows highest values for the thin films. An increase of thickness over the critical results in growth of the layers with almost thickness-independent relaxed lattice constant, so the slope of the LCV dependence on thickness decreases (Fig. 9d). The LCV value for the 3DGE $CeO_2$ films grown at high deposition rate, is much higher than that of films on standard (110) NGO substrates, but we note that with an increase of thickness the LCV of 3DGE films decreases to 1.2%, close to the value of ~1%, obtained for the standard-oriented films of similar thickness (Fig. 3). We may assume that the spread of the c lattice constant is mainly present in the bottom part of the film, and the top, presumably relaxed, layer is more homogeneous.

The orientation of the films grown at high deposition rate strongly (up to -3º) deviates from the calculated value (Fig. 9a). We have no good explanation for this phenomena and the deviation decreases with film thickness. Assuming 3DGE mechanism of this tilt formation, we can calculate the step heights coefficient $k = c_f \ / \ c_s = 1.21$, resulting in the observed tilt angle of ~22º. The corresponding film step height $c_f$ is ~4.68 Å, or the substrate step height should change to 4.47 Å. No obvious matches were found for these translational distances in the family of (Nd,Ga,Ce)Ox oxides, so probably this tilt is not a result of chemical interaction between the film and the substrate. An increase of thickness, though, brings the film orientation into the usual 3DGE range (completely strained growth with a small negative deviation), and for thicknesses ~800 Å the film orientation reaches the "standard" value calculated using Eq. (2) (Fig. 9a). The surface of the growing film in a multilayer structure inherits the system of steps from the bottom layer - and from the substrate surface - so the orientation of the top layer follows the formula (2) as if the top layer is deposited directly on the substrate surface (see, for example, the $YBa_2Cu_3O_x/BaZrO_3/NdGaO_3$ heterostructures in [1]), if the growth mechanism is limited to the 3DGE mode and no secondary effects influence the multilayer. This inheritance of the steps on the surface explains evolution of the 3DGE $CeO_2$ film orientation with thickness: the top relaxed layer grows over the bottom strained layer with the same 3DGE matching relations, transforming tilt of the strained film (step height $c_f$ = 5.258 Å) into the tilt of the relaxed film ($c_f$ = 5.41 Å, taking into account oxygen depletion at high deposition rate). The mis-orientation of the crystallites of the films grown at high deposition rate is somewhat smaller (~1.4º) than for the low-rate films, but also remains almost constant for all thicknesses (Fig. 9b, closed symbols). This confirms our assumption of 3DGE mechanism of change of film tilt with thickness: the spread of orientations of the crystallites of the film is set by initial seeding, and then all crystallites tilt with the change of the step height in a uniform manner, conserving the overall spread of crystallites orientations and, hence, the measured FWHM of the rocking curve.

The common (thickness + deposition rate) nature of the dependences of Fig. 9 can be illustrated by the points at ~500 Å. The samples with this thickness were deposited to the highest thickness among the low-deposition-rate samples, but, at the same time, they were deposited at the highest deposition rates in this group of samples. As a consequence, the points at ~500 Å can be added to the high-rate data on Figures 9a, b, d, without significant discrepancy with the observed dependences, and even on Fig. 9c the measured c value lays withins the high spread of measured lattice constants for the high-rate samples with thickness of 400 Å.

The saturation of the growing film with oxygen depends not just on the momentary deposition rate during PLD, but also on the relaxation time as given by the period between the laser pulses. This is illustrated by Fig. 10, where a decrease of the repetition rate from 1 to 0.3 Hz at a constant momentary deposition rate of 3 Å/pulse results in a change from formation of a film with a significant

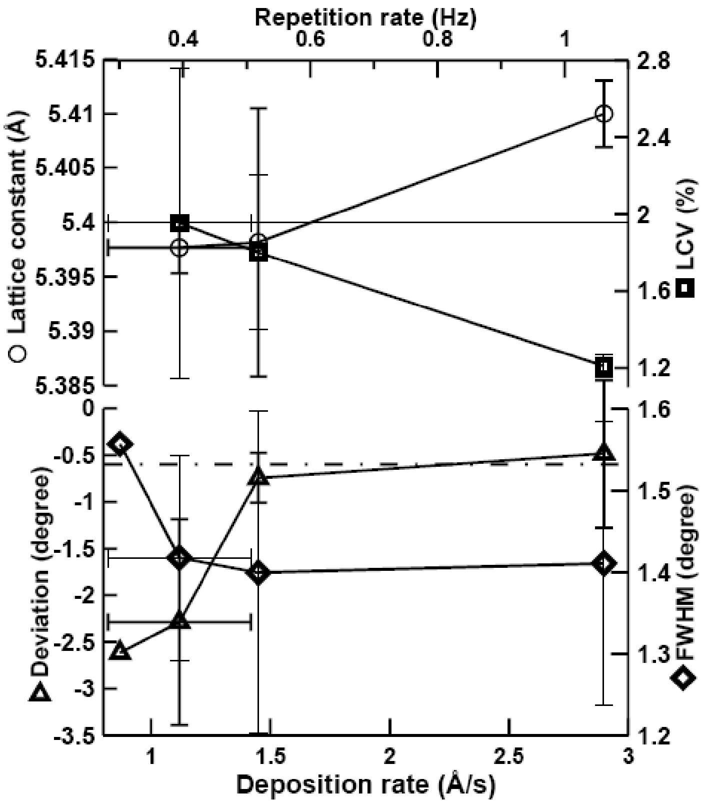

Figure 10. Dependences of properties of 3DGE $CeO_2$ films on the average deposition rate. Standard deposition conditions, the substrate tilt angle 18.43º, the momentary deposition rate is 3 Å/pulse. The data at 0.4 Hz (1.12 Å/s) are complemented with two samples from other data sets with similar momentary deposition rate and thickness parameters.

density of oxygen vacancies (lattice constant 5.41±0.025 Å) to the growth of an almost completely oxygenated film (5.398 Å).

Again, we cannot completely resolve the effects of deposition rate and thickness; the samples fabricated at 0.5 Hz (1.45 Å/pulse) are ~300 Å thick, while samples with a lower repetition rate are thinner and with a higher repetition rate are more thick. As a consequence, the dependences on repetition rate in general repeat the thickness dependences of Fig. 9, high-rate samples. This additionally refined data set still provides some more information on the growth of the 3DGE $CeO_2$ films. The ~300 Å thickness, similarly to the films on (110) NGO substrates, seems to be the border between two layers of the film. The thin films show higher mis-orientation of crystallites and a strong deviation from the calculated 3DGE orientation. Both effects gradually decrease with thickness and at the critical thickness the deviation reaches the level typical for the completely strained films (dash-dotted line, bottom graph of Fig. 10), while FWHM saturates at ~1.4º. The lattice constant below the critical thickness seems to be almost constant; we attribute this to the complex effect of more complete oxygenation, decreasing c value, and of more complete relaxation during longer periods between the laser pulses, providing lower level of the substrate-induced strain and, hence, smaller contraction of c lattice constant. The effect of the substrate-induced strain cannot be neglected, as can be seen from the LCV dependence: the variation of the lattice constant is higher for thin films, revealing relaxation of the strain with thickness. The spread of the LCV parameter from sample to sample (error bars on Fig. 10) rapidly decreases with thickness, implying reproducible growth of a relaxed $CeO_2$ from the critical thickness of the film.

Summarizing, the thickness dependences reveal three possible structures of the 3DGE $CeO_2$ films, depending on the deposition rate:

- very low deposition rate: the film grows completely oxygenated and relaxes all strain introduced by substrate mismatch in the very beginning of deposition. As a consequence, the orientation of the film corresponds to the 3DGE formula with relaxed c, but the crystallites of the film are strongly mis-oriented (the FWHM is up to 2.6º);
- low deposition rate: the film is completely oxygenated, and grows completely-strained, with a significant contraction of the c lattice constant due to the biaxial tensile substrate-induced strain. The orientation of the film follows the 3DGE relation with contracted *c* as the step height of the film, the spread of the crystallites orientations is independent on thickness in the studied range and shows much smaller values than that of the films grown at very low deposition rate;
- high deposition rate: the film presumably consists of a strained bottom part and the relaxed top layer, with a critical thickness about 300 Å. The lattice constant of the relaxed part reveals insufficient oxygenation of the film during growth. The orientation of the film evolves with thickness from a very high negative deviation for thin films, through the orientations typical for the completely-strained films at medium thickness, and to the orientation well matching the 3DGE relation for the step height equal to the lattice constant of the relaxed film. The mis-orientation of crystallites decreases with thickness and saturates at critical thickness at a level somewhat smaller than that of the low-rate films.

## 4. CONCLUSIONS

In summary, the deposition of $CeO_2$ thin films on NGO TAS by PLD usually results in the formation of tilted-axes films with the tilt angle following the 3DGE tangent dependence. The deviations from the geometrical formula can be divided into a systematic negative part and local deviations around certain film tilt angles. The width of the rocking curve and the lattice constant variation for the 3DGE $CeO_2$ films increase almost linearly with tilt angle until $\gamma$ = 19º (film tilt $\gamma' \approx$ 24º).

The systematic deviation is present already for very thin films and may be explained as the effect of completely-strained coherent growth of the bottom layers of $CeO_2$ film on the NGO substrate. The biaxial distortion of the $CeO_2$ lattice results in contraction of the out-of-plane lattice constant c, with corresponding decrease of the growth step and the tilt angle of the film. A simple volume-preserving assumption provides excellent agreement with the measured values.

The minimization of the surface energy when the film surface is aligned with a SICP, namely, (012) at $\gamma'$ = 26.6º and (013) at 18.4º, may be proposed as an explanation for the local deviations from the calculated dependence.

The macroscopic structure of the 3DGE $CeO_2$ films generally repeats the structure of the $CeO_2$ films on the standard (110)-oriented NGO substrates. The deposition rate influences the growth of 3DGE $CeO_2$ films in two ways: an increase of deposition rate results in an insufficient oxygenation of the Ce atoms arriving of the substrate surface, while a decrease of deposition rate provides more time for relaxation of the substrate-induced strain in the film. As a consequence, at different deposition rates the film exhibits three possible structures: (i) relaxed completely oxygenated film at very low deposition rate, (ii) completely strained well-oxygenated film at moderate deposition rates, and (iii) oxygen-deficient film consisting of two layers at high deposition rates. The deviations of orientation of the film from the 3DGE formula are set by the lattice constant c in the direction normal to the (110) SICP of the substrate, which, in turn, depends on oxygen deficiency and the level of strain, introduced into the film by lattice mismatch with the substrate.

## ACKNOWLEDGMENTS

The work was supported by Program of Ministry of Science and Higher Education of Russian Federation. I.K.B. wishes to acknowledge FCT for its financial support (grant IF/00582/2015).

## REFERENCES

[1] P. B. Mozhaev, J. E. Mozhaeva, A. V. Khoryushin, J. Bindslev Hansen, C. S. Jacobsen, I. K. Bdikin, I. M. Kotelyanskii, V. A. Luzanov, Three-dimensional graphoepitaxial growth of oxide films by pulsed laser deposition, *Phys. Rev. Materials*, **2** 103401 (2018).
[2] O. Igarashi, Crystallographic Orientations and Interfacial Mismatches of Single-Crystal CdS Films Deposited on Various Faces of Zinc-Blende-Type Materials, *J. Appl. Phys.* **42,** 4035-4043 (1971).

[3] M. Aindow and R.C. Pond, On epitaxial misorientations, *Philos. Mag. A*, **63**, 667-694 (1991).

[4] F. Riesz, Crystallographic tilting in lattice-mismatched heteroepitaxy: A Dodson–Tsao relaxation approach, *J. Appl. Phys.* **79,** 4111-4117 (1996).

[5] J. P. Hirth and R. C. Pond, Strains and Rotations in Thin Deposited Films. *Philos. Mag.*, **90**, 3129-3147 (2010).

[6] H. Nagai, Structure of vapor-deposited $GaxIn_{1-x}As$ crystals, *J. Appl. Phys.* **45**, 3789-3794 (1974).

[7] I. K. Bdikin, P. B. Mozhaev, G. A. Ovsyannikov, F. V. Komissinskii, I. M. Kotelyanskii, and E. I. Raksha, The growth and domain structure of YBa2Cu3Ox films on neodymium gallate substrates with a deviation of the normal to the surface from the [110] direction in NdGaO3, *Phys. Solid State*, **43**, 1611-1620 (2001).

[8] I. K. Bdikin, P. B. Mozhaev, G. A. Ovsyannikov, P. V. Komissinski, and I. M. Kotelyanskii, Growth and domain structure of YBa2Cu3Ox thin films and YBa2Cu3Ox/CeO2 heterostructures on tilted NdGaO3 substrates, *Physica C*, **377**, 26-35 (2002).

[9] P. B. Mozhaev, J. E. Mozhaeva, I. K. Bdikin, I. M. Kotelyanskii, V. A. Luzanov, J. Bindslev Hansen, C. S. Jacobsen, and A. L. Kholkin, Out-of-substrate plane orientation control of thin YBa2Cu3Ox films on NdGaO3 tilted-axes substrates, *Physica C*, **434**, 105-114 (2006).

[10] J. D. Budai, W. Yang, N. Tamura, J.-S. Chung, J. Z. Tischler, B. C. Larson, G. E. Ice, Ch. Park, and D. P. Norton, X-ray microdiffraction study of growth modes and crystallographic tilts in oxide films on metal substrates, *Nature Mater.*, **2**, 487-492 (2003).

[11] V. F. Solovyov, K. Develos-Bagarinao, D. Nykypanchuk, Nanoscale abnormal grain growth in (001) epitaxial ceria, *Phys Rev B*, **80,** 104102 (2009).

[12] R. Lyonnet, A. Khodan, A. Barthelemy, J.-P. Contour, O. Durand, J.L. Maurice, D. Michel, J. De Teresa, Pulsed Laser Deposition of $Zr_{1-x}Ce_xO_2$ and $Ce_{1-x}La_xO_{2-x/2}$ for Buffer Layers and Insulating Barrier in Oxide Heterostructures, *J. of Electroceramics* **4,** 369-377 (2000).

[13] M.A.A.M. van Wijck, M.A.J. Verhoeven, E.M.C.M. Reuvekamp, G.J. Gerritsma, D.H.A. Blank, H. Rogalla, CeO2 as insulation layer in high Tc superconducting multilayer and crossover structures, *Appl. Phys. Lett.* **68,** 553-555 (1996).

[14] P.C. McIntyre, B.P. Chang, N. Sonnenberg, M.J. Cima, Defect Formation in Epitaxial Oxide Dielectric Layers Due to Substrate Surface Relief, *J. of Electronic Mater.*, **24,** 735-745 (1995).

[15] P. B. Mozhaev, A. V. Khoryushin, J. E. Mozhaeva, J.-C. Grivel, J. Bindslev Hansen, C. S. Jacobsen, Pulsed Laser Deposition of YBa2Cu3Ox with Scanning Beam: Target to Substrate Composition Transfer and Film Structure, *J. Supercond. Novel Magnetism*, **30**, 2401-2428 (2017).

[16] P.B. Mozhaev, G.A. Ovsyannikov, J.L. Skov, Influence of laser ablation parameters on buffer CeO2 layer on sapphire orientation and on superconducting YBa2Cu3Ox thin film properties, *Technical Physics (Zhurnal Tehnicheskoj Fizika)*, **44,** 242-245 (1999).

[17] P.B. Mozhaev, J.E. Mozhaeva, C.S. Jacobsen, J. Bindslev Hansen, I.K. Bdikin, V.A. Luzanov, I.M. Kotelyanskii, S.G. Zybtsev, Bi-epitaxial YBa2Cu3Ox Thin Films on Tilted-axes NdGaO3 Substrates with CeO2 Seeding Layer, *Proceedings of EUCAS'05, IOP Conf Series*, **v. 43**, iss. 1, pp. 1119-1122 (2006).

[18] P.B. Mozhaev, J.E. Mozhaeva, I.K. Bdikin, I.M. Kotelyanskii, V.A. Luzanov, S.G. Zybtsev, J. Bindslev Hansen, C.S. Jacobsen, Out-of-plane tilted Josephson junctions of bi-epitaxial YBa2Cu3Ox thin films on tilted-axes NdGaO3 substrates with CeO2 seeding layer, Proceedings of WWS'05, *Physica C*, **v. 435**, pp. 23-26 (2006).

[19] A.V. Khoryushin, P.B. Mozhaev, J.E. Mozhaeva, I.K. Bdikin, Y. Zhao, N.H. Andersen, C.S. Jacobsen, J.B. Hansen, Substrate decoration for improvement of current-carrying capabilities of YBa2Cu3Ox thin films, *Physica C*, **486,** 1-8 (2013).

**NANOMATERIALS**
**SCIENCE & ENGINEERING**
Vol. 2, No. 2, pp. 74-82 (2020)

RESEARCH ARTICLE

https://doi.org/10.34624/nmse.v2i2.11175

# Structured superhydrophilic coatings made from aminomalononitrile

**Rou Jun Toh[1], Richard Evans [1], Helmut Thissen [1], Nicolas H. Voelcker [1,2,3], Marco D'ischia [4] and Vincent Ball [5,6,*]**

*[1] CSIRO Manufacturing, Research Way, Clayton 3168, Victoria, Australia*
*[2] Monash University, Monash Institute of Pharmaceutical Sciences, 381 Royal Parade, Parkville, 3052, Victoria, Australia*
*[3] Leibniz Institute for New Materials, Campus D2, 66123 Saarbrücken, Germany.*
*[4] Department of Chemical Sciences, University of Naples Federico II, Via Cinthia 26, 80126 Naples, Italy*
*[5] Université de Strasbourg, Faculté de Chirurgie Dentaire, 8 Rue Sainte Elizabeth, 67000 Strasbourg, France*
*[6] Institut National de la Santé et de la Recherche Médicale, Unité Mixte de Recherche 1121, 11 Rue Humann, 67085 Strasbourg, Cédex, France*
** corresponding author: vball@unistra.fr*

Received 19 November 2019; accepted 21 May 2020; published online 10 June

## ABSTRACT

The motivation for new versatile and biocompatible coatings incites researchers to try to copy solutions developed by living organisms like mussels able to adhere to all kinds of substrates in wet conditions. Another source of inspiration may be found in molecules containing reactive CN groups which have been formed in prebiotic conditions on the early formed Earth. Among such molecules, aminomalonitrile (AMN) has been shown to allow the formation of coatings on all kinds of known materials. In the present investigation, the deposition mechanism of AMN based coatings on silicon, quartz and glass is investigated. It is shown that the film deposition is preceded by a lag phase during which AMN undergoes already a transformation in solution. The obtained coatings undergo a morphological transition from islands to fibrillar structures with a concomitant change in composition and hydrophilicity. A putative structure based on X-ray photoelectron spectroscopy data is proposed for the AMN based films deposited at the solid-water interface.

## 1. INTRODUCTION

Owing to the substrate specificity of most surface coating methodologies, surface scientists are investigating versatile surface chemistries. One major source of inspiration consists in biomimicry of mussel foot proteins (mefps) [1]. Indeed mussels are able to adhere to almost all known materials even in wet conditions and to withstand strong shear stresses which is a requirement for their survival. The composition of mefps, rich in L-lysine and in the non-natural amino acid L-DOPA, incited to use dopamine, containing an amino group as in L-Lysine and a catechol group as in L-DOPA, as a candidate to produce versatile and robust coatings in oxidative conditions [2, 3]. This led to the reproducible deposition of polydopamine films able to undergo easy secondary functionalisation through reaction with nucleophiles [4] or with metal nanoparticles [2, 5] after reduction of metallic cations. Those polydopamine films are known to be useful for a lot of applications as coatings for biomaterials and for energy conversion processes [6]. Recently it was shown that inspiration from suspected prebiotic processes allows also to deposit conformal coatings on almost all known materials [7, 8] with application fields similar to those of polydopamine. The used precursor of such coatings is aminomalonitrile (AMN) which undergoes self- assembly and surface deposition after neutralisation of is para-toluenesulfonate salt in basic conditions. It is the aim of this article to summarize our mechanistic investigations [9] on the deposition of AMN based coatings and to show that those films also form at water-air interfaces and can be transferred on solid substrates via the

Langmuir–Schaeffer [10] horizontal transfer method. Most importantly, we will show that the AMN based colloids formed in solution, the films deposited at the water-solid interface and those deposited at the water-air interface are different. Additionally, the coatings deposited at the water-solid interface become superhydrophilic after a critical deposition time decreasing upon an increase in the AMN concentration.

## 2. MATERIALS AND METHODS

### *Chemicals*

Aminomalononitrile-*para*-toluenesulfonate (AMN, ref. 221147), sodium hydrogen phosphate (ref. S-9638) and potassium hexacyanoferrate (ref. P9387) were purchased from Sigma-Aldrich and used without purification. All solutions were made from MilliQ water ($\rho$ = 18.2 MΩ·cm, Millipore). AMN was dissolved in 50 mM sodium phosphate buffer at pH = 7.5 at concentrations ranging from 5 to 40 $mg \cdot mL^{-1}$ corresponding to molar concentrations ranging from 19.7 mM to 158 mM. The reaction was triggered by adjusting the pH of these solutions to 8.6 ± 0.1 with a concentrated sodium hydroxide solution. Immediately after pH adjustment, cleaned samples to be coated were immersed in the AMN solution. The pH of all solutions was measured with a three point calibrated Hi221 pH meter (Hanna Instruments).

### *Substrate materials*

AMN films were deposited on quartz, glass and silicon wafer samples, for characterization by means of UV-Vis spectroscopy, Langmuir-Blodgett transfer and ellipsometry, respectively. All of these substrates were cleaned in the same manner, just before deposition process. They were rinsed with ethanol, dried with a filtrated air flow and subjected to 15 min of $O_2$ plasma cleaning (PDC-32G-2, Harrick Scientific, USA).

### *UV-Vis spectroscopy*

UV-Vis spectra of the AMN based films deposited on plasma cleaned quartz slides where obtained against a pristine cleaned quartz slide as a reference using a double beam mc² spectrophotometer (Safas, Monaco, France). The same spectrophotometer was used to measure the spectra of AMN solutions after different reaction times and appropriate dilution with sodium phosphate buffer, using the pure buffer as the reference. The solutions were contained in ethanol cleaned quartz cuvettes , 1 cm optical path (Thuet, Blodeslheim, France).

### *Ellipsometry*

The AMN based films deposited for a reaction time *t* on freshly cleaned silicon substrates (featuring a naturally grown silicon dioxyde layer about 2 nm in thickness) were characterized by constant wavelength (632.8 nm) ellipsometry at a constant angle of incidence (70°) using a PZ 2000 ellipsometer (Horiba, France). For the calculation of the film thickness from the measured ellipsometric angles, the real part of the refractive index was fixed to 1.6 whereas its imaginary part was fixed equal to 0 owing to the film transparency at the used wavelength. The given thickness values are the average of 5 measurements (± one standard deviation) on regularly spaced spots along the major axis of the used wafer.

### *X-ray photoelectron spectroscopy (XPS)*

The analysis of the AMN coated silicon slides was performed using an AXIS Ultra DLD spectrometer (Kratos Analytical, Manchester, UK) with a monochromated Al Kα source at a power of 168 W and a hemispherical analyser operating in the fixed analyser transmission mode and the standard aperture. The sample analysis area was 0.3 mm × 0.7 mm. Survey spectra were obtained at a pass energy of 160 eV. CasaXPS processing software version 2.3.15 (Casa Software Ltd., Teignmouth, UK) was used to perform data processing, with all elements present being identified from survey spectra. Calculation of the atomic concentrations of the detected elements were derived from integral peak intensities and the sensitivity factors supplied by the manufacturer.

### *Scanning electron microscopy (SEM)*

SEM images were acquired by a Zeiss Gemini SEM 450 (Zeiss, Germany) at an acceleration voltage of 5 kV. Energy-dispersive X-ray spectroscopy (EDS) was carried out with an X-Max EDS system (Oxford Instruments, Oxford, UK) at an acceleration voltage of 15 kV. More details can be found in ref. [9].

### *Atomic force microscopy (AFM)*

AMN based films deposited on silicon wafers from 10 mg·mL$^{-1}$ AMN solutions were rinsed with distilled water and dried under a stream of filtered air before imaging in the contact mode with a MLCT-C cantilever (nominal spring constant = 10 mN·m$^{-1}$ ) using a Nanoscope III atomic force microscope (Bruker, Mannheim, Germany). Images were analysed with the Nanoscope Analysis software to determine the mean squared roughness of the AMN based films.

### *Contact angle measurements*

For static water contact angle measurements, 5 µL distilled water was put on the surface of AMN based films deposited on plasma cleaned quartz slides. The contact angle was measured after 10 s using an Attension Theta goniometer (Biolin Scientific, Sweden). At least ten measurements were averaged to get a reliable value.

### *Langmuir-Schaeffer transfer of AMN based films from the liquid-air interface*

AMN films were grown for 16 h or 23 h at the liquid-air interface from a 10 mg·mL$^{-1}$ AMN solution. Part of the film was aspirated by a pipette and a cleaned glass slide mounted horizontally on a sample holder was immersed below the freshly created uncovered liquid-air interface, starting from the freed interface. The slide was then put below the apparent AMN film and the sample holder was removed in the upwards direction with a speed of 0.002 cm·s$^{-1}$. The films were then rinsed with pure water and dried under a flow of filtered air before AFM imaging in the dry state and in the contact mode as previously described.

## 2. RESULTS AND DISCUSSION

The initial pH of the AMN salt solution was lower than the initial pH of the 50 mM sodium phosphate buffer in an AMN concentration dependant manner.

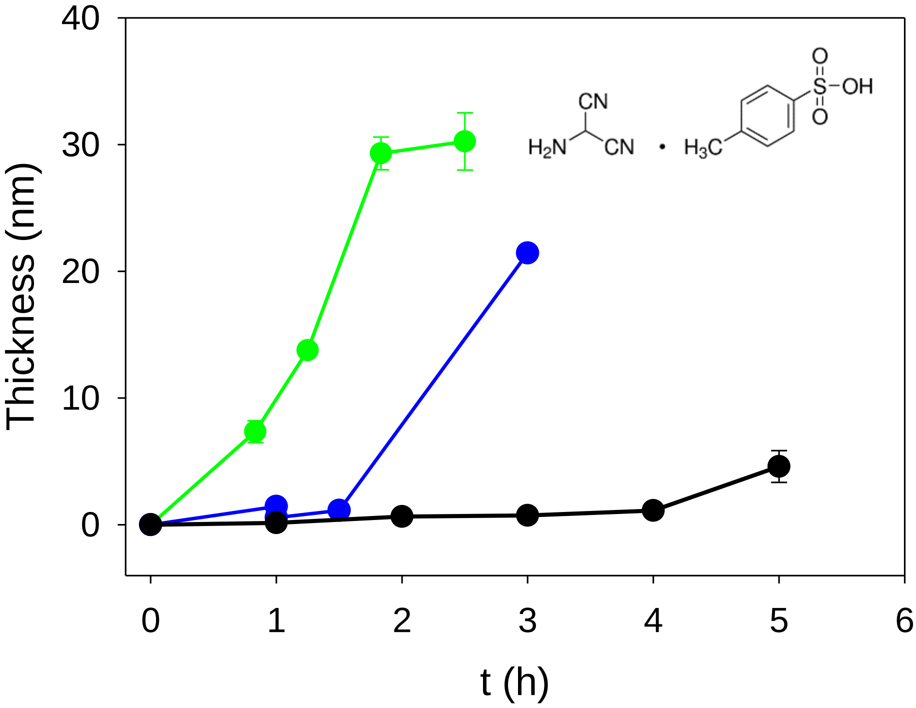

Figure 1. AMN based film thickness as measured by ellipsometry on silicon substrates from AMN solutions (initial pH = 8.6) at 5 (——), 10 (——) and 20 (——) mg.mL$^{-1}$. Each data point corresponds to an individual substrate and to the average ± one standard deviation over 5 different locations. The inset represents the structure of the used AMN salt. Modified from ref. [9] with authorization.

This decrease in pH stabilized AMN with respect to chemical transformation [9]. However titration of the AMN containing solutions to 8.6 with sodium hydroxide initiated a coloration change of the solution and a progressive deposition of a coating on both the reaction beaker and on the substrates immersed in it. The film deposition on solid substrates was delayed by an AMN concentration dependant lag phase as observed by means of single wavelength ellipsometry (Figure 1), UV-visible spectroscopy and quartz crystal microbalance with dissipation monitoring (data not shown, see ref.[9].

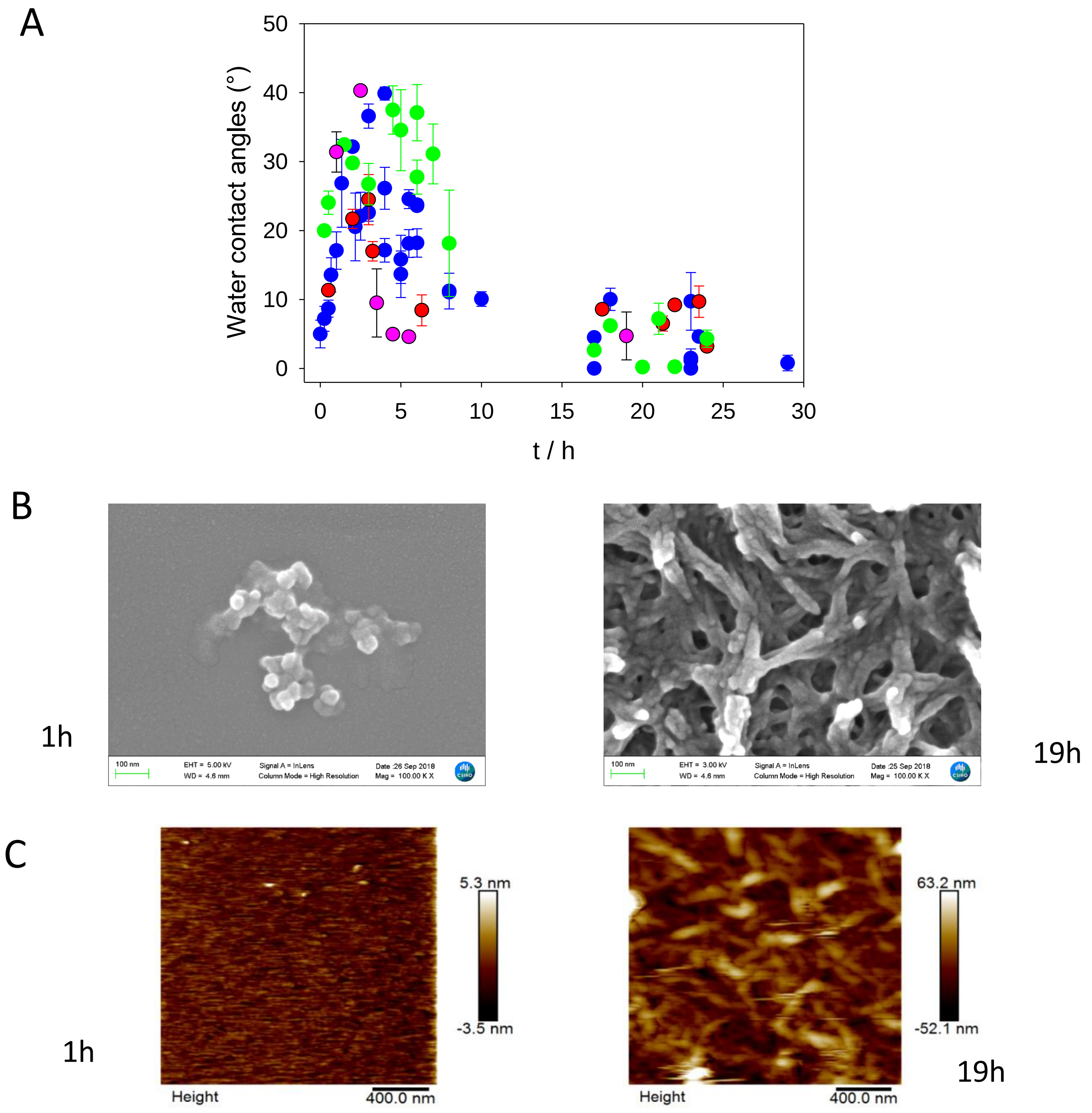

Figure 2. A : Static water contact angles of AMN based coatings as a function of time for different AMN concentrations : 5 (●), 10 (●), 20 (●) and 40 (●) mg·mL$^{-1}$.
B: Film morphology of AMN based coatings after 1 and 19 h of deposition from a 10 mg·mL$^{-1}$ AMN solution as obtained by SEM.
C: Film morphology of AMN based coatings after 1 h and 19 h of deposition from a 10 mg·mL$^{-1}$ AMN solution as obtained by contact mode AFM. The image size is 2 µm x 2 µm.

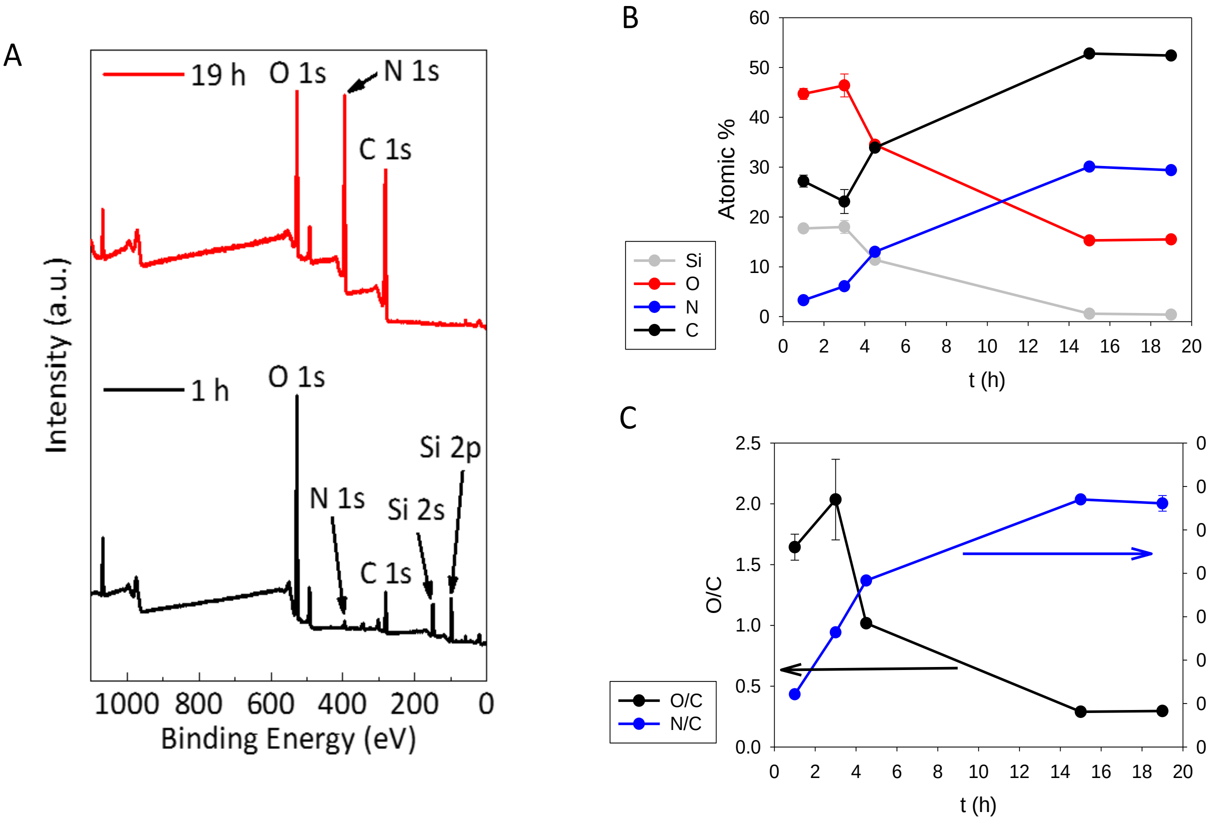

Figure 3. A: XPS survey spectra of AMN based films after different deposition times (1 h and 19 h) on glass slides.
B: Evolution of the atomic percentage of Si (●), O (●), N (●) and C (●) as a function of time for AMN based coatings deposited in a 10 mg·mL$^{-1}$ solution. The coatings were deposited on glass slides.
C: Evolution of the O/C (●) and N/C (●) ratios with reaction time in a 10 mg·mL$^{-1}$ AMN solution. The error bars correspond to ± one standard deviation. Modified from ref. [9] with authorization.

The static water contact angles of the AMN based films passed through a maximum at intermediate deposition times and became progressively superhydrophilic (water contact angles lower than 10°) after intermediate deposition times. The higher the initial AMN concentration, the faster the superhydrophilic regime is reached (Figure 2 A). Such changes in surface wettability may be attributed to composition and/or surface roughness changes [11]. Concerning the surface topography of the AMN based coatings, SEM (Figure 2B) and AFM imaging (Figure 2C) clearly reveal an increase in surface roughness associated with the formation of fibrillary structures from initially deposited clusters (Figure 2B). Those fibrillar structures are formed after a few hours in the absence of any template suggesting the self-assembly of anisotropic building blocks formed upon the reaction.

The morphology change is accompagnied by a modification in surface composition as shown by XPS spectroscopy (Figure 3). With increasing the deposition time, whatever the initial AMN concentration, the Si2S and Si2p photoelectrons due to the silicon substrates are not detected anymore highlighting the formation of conformal coatings. Those coatings were also found impermeable to a redox probe like potassium hexacyanoferrate [9]. Analysis of the obtained XPS spectra also reveals a progressive decrease of the O content of the films up to a constant value (Figure 3). Since O is present in the $SiO_2$ oxide film grown spontaneously on silicon, and since Si is not detected anymore when the O content reaches a steady state value, this means that the AMN based

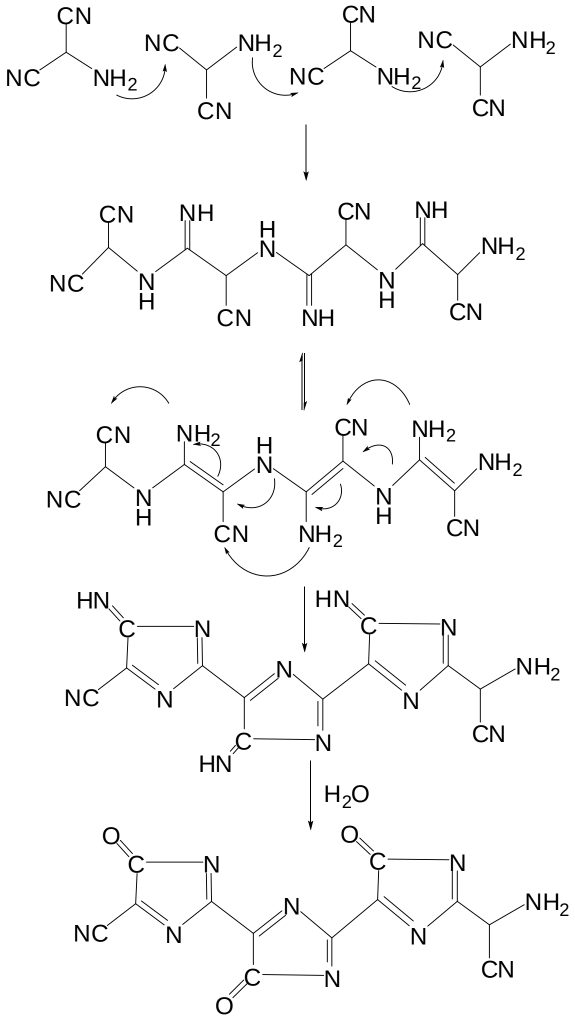

General formula: $(C_3N_2O)_n$

N/C = 0.66
O/C = 0.33

Scheme 1. Proposed structure of the polymeric material obtained at the solid-liquid interface from an AMN based solution at an initial pH of 8.6. Reproduced from ref.[9] with authorization.

films incorporate O which is not present in the AMN monomer (inset in Figure 1). This finding is important for inferring the film formation mechanism as described later on. The film deposition is also characterized by an increase in the surface concentration of C and N (Figure 3B). Interestingly the N/C atomic ration reaches a constant value of about 0.57 after prolonged deposition time (even if the film continues to grow up to this point) as in a previous investigation [7]. This C/N value is lower than the corresponding value for the AMN monomer which is equal to 1 (inset of Figure 1). This important finding means that some N is lost during the film deposition independently from the CN- release detected in QCM-D experiments performed on gold: indeed a loss of film is detected with this gravimetric method when a gold substrate is put in contact with an AMN solution at an initial pH value of 8.6, meaning a release of CN- and subsequent partial dissolution of gold.

The simultaneous incorporation of O in the film and the C/N ratio close to 0.6 is interpreted by an hydrolysis reaction of the initially deposited film as shown in scheme 1 where the putative structure of the obtained material in given. Such a structure needs of course to be confirmed in future investigations.

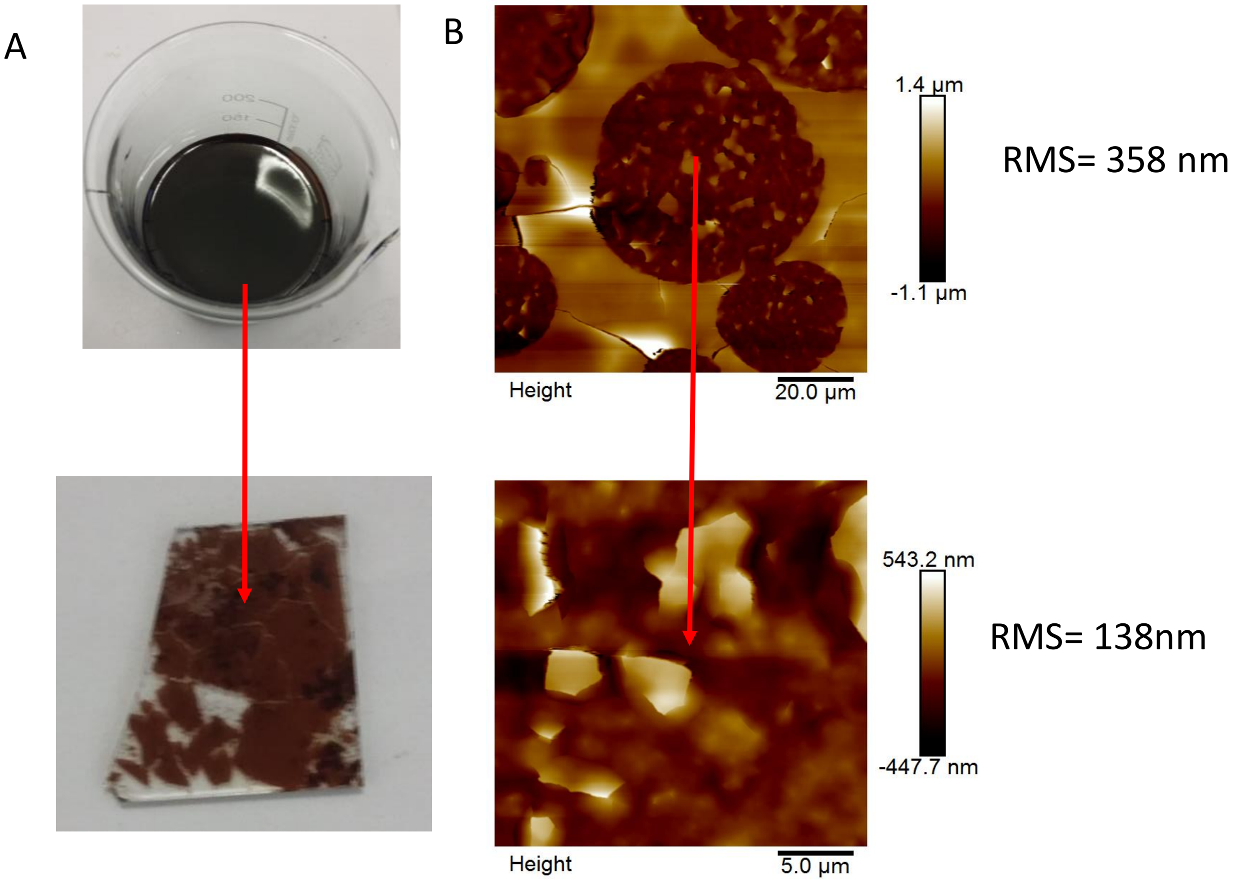

Figure 4. A: AMN based films on the liquid-air interface after 16 h of reaction (AMN at 10 $mg\cdot mL^{-1}$ at an initial pH of 8.6). Picture of the surface of the AMN containing solution after 16 h and after Langmuir Schaeffer transfer on a cleaned glass slide.
B: AFM surface topographies of the transferred AMN based film, the image size being 100 µm x 100 µm and 25 µm x 25 µm, respectively. The red arrow points to the region of the first image from which the image having a 25 µm x 25 µm size was acquired. Modified from ref. [9] with authorization.

Interestingly we also find that an AMN based film forms progressively on the water-air interface provided the AMN solution is not shaken (Figure 4A). This finding is in strong analogy with the situation of dopamine solutions in the presence of an oxidant [12] and strongly suggests that the the hydrophilic AMN transforms into amphiphilic structures which can self-assemble at the water-air interface. The final structure proposed in Scheme 1 is clearly amphiphilic with a hydrophobic chain decorated with hydrophilic CO groups. Those films deposited at the water-air interface can be transferred on cleaned glass slides through the Langmuir –Schaeffer method [10] and their morphology is drastically different (Figure 4b) than the morphology of AMN based films directly deposited on glass at the solid-water interface (Figure 2 B and C).

This finding suggests that the AMN film deposition mechanism is different at the solid-water and at the water –air interfaces, a point which clearly deserves further investigations. Complementarily, UV-visible spectra taken on quartz slides after a given duration of deposition and on diluted AMN containing solutions after the same reaction time are different (Figure 5A). This shows clearly that the film structure and / or composition is different than the composition of the AMN containing solution in which colloids form progressively with time, ending up with the sedimentation of precipitates. The evolution of AMN in solution proceeds also without a lag phase, contrarily to the film deposition (blue curve in Figure 5A, in agreement with the findings displayed in Figure 1).

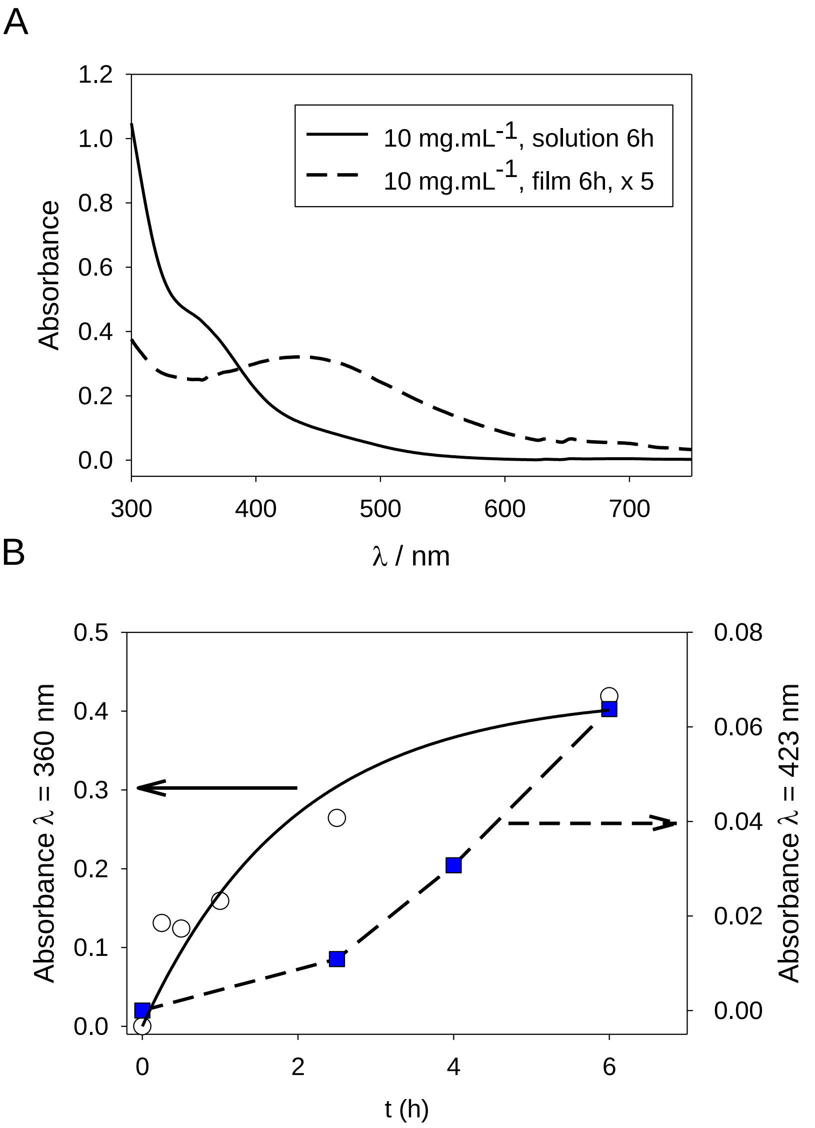

Figure 5. A: UV-Vis spectra of a 10 mg·mL$^{-1}$ AMN solution (——) after 6 h of reaction and of an AMN film (– – – –) deposited on a quartz wafer after the same reaction time, scaled by a factor of 5.
B: Time evolution of the absorbance at λ=360 nm (—○—, left hand vertical axis) and at λ=423 nm (– – –■– – –, right hand vertical axis) in the case of an AMN solution at 10 mg·mL$^{-1}$ and for an AMN based film deposited from the same solution, respectively. Reproduced from ref.[9] with authorization.

## 4. CONCLUSIONS

The chemical evolution of the para-toluenesulfonate salt of AMN after its neutralization leads to the formation of conformal films on all kinds of substrates. Herein we focused on the film formation mechanism on quartz and glass substrates. It is found that the film deposition is preceeded by a lag phase whereas the chemical evolution of AMN in solution proceeds via a continuous pathway (Figure 5B). The obtained coatings at the solid-water interface undergo a morphological transition from islands to fibrillary structures accompagnied with the appearance of a superhydrophilic water wettability regime (Figure 3). In the same time the film composition changes (Figure 4). This lead us to propose a putative chemical structure compatible with the XPS compositional analysis (Scheme 1). Finally, we found that the chemical evolution/structural evolution of AMN is different at the solid-water and water-air interfaces (Figure 4). Further investigations implying detailed NMR and X ray diffraction data (to relate the fibrillary film morphology to the self-assembly process) are required to understand the complex chemical pathways undergone by AMN in slightly alkaline solutions.

## REFERENCES

[1] B.P. Lee, P.B. Messersmith, J.N. Israelachvili and J.H. Waite, *Ann. Rev. Mater. Res.*, **41**, 99-132 (2011).
[2] H. Lee, S.M. Dellatore, W.M. Miller and P.B. Messersmith, *Science*, **318**, 426-430 (2007).
[3] F. Bernsmann, V. Ball, F. Addiego, A. Ponche, M. Michel, J.J. de Almeida Gracio, V. Toniazzo and D. Ruch, *Langmuir*, **27**, 2819-2825 (2011).
[4] H. Lee, J. Rho and P.B. Messersmith, *Adv. Mater.*, **21**, 431 (2009).
[5] M. Lin, H. Huang, Y. Liu, C. Liang, S. Fei, X. Chen and C. Ni, *Nanotechnology* , **24**, art. 065501 (2013)
[6] Y. Liu, K. Ai and L. Lu, *Chem. Rev.* **114**: 5057-5115 (2014).
[7] H. Thissen, A. Koegler, M. Salwiczek, C.D. Eaton, Y. Qu, T. Lithgow and R.A. Evans, *NPG Asia Mater.*, **7**, art. e225 (2015).
[8] D.J. Menzies, A. Ang H. Thissen and R.A. Evans, *ACS Biomater. Sci. Eng.*, **3**, 793-806 (2017).
[9] R.J. Toh, R.A. Evans, H. Thissen, N.H. Voelcker, M. d'Ischia and V. Ball, *Langmuir*, **35**, 9896-9903 (2019).
[10] I. Langmuir and V.J. Schaefer, *J. Amer. Chem. Soc.* **58**, 284-287 (1936).
[11] D. Quéré, *Ann. Rev. Mater. Sci.* **38**, 71-99 (2008).
[12] F. Ponzio, P. Payamyar, A. Schneider, M. Winterhalter, J. Bour, F. Addiégo, M.-P. Krafft, J. Hemmerlé and V. Ball, *J. Phys. Chem. Lett.* **5**, 3436-3440 (2014).

NANOMATERIALS
SCIENCE & ENGINEERING
Vol. 2, No. 2, pp. 83-92 (2020)

RESEARCH ARTICLE

https://doi.org/10.34624/nmse.v2i2.9711

# Modelling of the Piezoelectric and Pyroelectric properties of the Ferroelectric composites thin films based on the polyvinylidene fluoride (PVDF) with Graphene and Graphene Oxide layers and fibers

**Vladimir S. Bystrov[1, *], Maxim V. Silibin[2], Xiangjian Meng[3], Tie Lin[3], Hong Shen[3], Bobo Tian[3], Jianlu Wang[3], Dmitry V. Karpynsky[4], Anna V. Bystrova[1, 5], Ekaterina V. Paramonova[1]**

*[1]Institute of Mathematical Problems of Biology, Keldysh Institute of Applied Mathematics, RAS, 142290 Pushchino, Moscow region, Russia*
*[2]National Research University of Electronic Technology "MIET",124498 Moscow, Russia*
*[3]National Lab. Infrared Physics, Shanghai Institute of Technical Physics, CAS, Shanghai, China*
*[4]Scientific-Practical Materials Research Centre of NAS of Belarus, Minsk, Belarus*
*[5]Riga Technical University, Biomed. Eng. and Nanotechnology Inst., Riga, Latvia*

**Corresponding author, e-mail address: vsbys@mail.ru*

Received 3 December 2019; accepted 23 May 2020; published online 10 June

## ABSTRACT

Recent results in modelling and computational studies of new composite nanomaterials based on polymer ferroelectrics and graphene/graphene oxide structures are reviewed. Main findings of the computational molecular modelling and calculations of the plane layered and fibers nanostructures, as well as multi-layered structures, and the piezoelectric and pyroelectric properties of the composites, consisting of polyvinylidene fluoride (PVDF) thin films and graphene/graphene oxide are analysed. The piezoelectric and pyroelectric effects were modelled, both piezo- and pyro-electric coefficients were calculated for several models, using various methods from HyperChem software tool, including molecular dynamics (MD) simulation with quantum-chemical semi-empirical PM3 method. The results obtained provide important insights into our understanding of the mechanisms of piezoelectricity and pyroelectricity in these new nanocomposites, give us new perspectives for further studies of the ferroelectric polymer-graphene nanomaterials.

## 1. INTRODUCTION

Polymer ferroelectrics, such as polyvinylidene fluoride (PVDF) and its copolymers, have a set of common ferroelectric properties [1-3]. These properties have many practical applications, and most of them connected with piezoelectricity and pyroelectricity [1-7]. Among various types of polymer ferroelectrics, thin ferroelectric films fabricated by spin coating technique or by Langmuir-Blodgett (LB) methods are especially interesting [3]. These films have unique mechanical flexible properties which are very important for many applications, including biomedical ones. These properties are also characteristic to more complex composite ferroelectric materials and films based on polymer ferroelectrics combined with graphene (G) and graphene oxides (GO) [6, 8, 9], which are presented in [6-11]. These materials have a unique combination of ferroelectric properties (high polarization and its switchable properties, piezo- and pyroelectricity, etc.) and have high elastic and mechanical characteristics [11]. Polymer ferroelectrics PVDF and their copolymers, such as poly(vinylidene fluoride-trifluoroethylene) P(VDF-TrFE) [2, 3, 12], especially in the form of thin highly-ordered Langmuir-Blodgett (LB) films [3, 13, 14], are thoroughly studied (both experimentally and theoretically) [12-21]. Computational molecular modeling and calculations of physical properties of such ferroelectric polymers, were performed using HyperChem package [22] which contains semi-empirical quantum-chemical method PM3 as well as some other methods and approaches [19-22]. So, on the basis of the molecular models proposed and developed in [19], the approaches and algorithms were developed to describe piezoelectric properties in materials, such as PVDF and P(VDF-TrFE), and calculations of the piezoelectric coefficients were performed [20]. Then, using the method of molecular dynamics (MD) the mechanisms of polarization switching in such polymer ferroelectrics were investigated [12, 21], by quantum calculations by PM3 approximation at each step of MD run.

Further attempts to incorporate graphene-like structures (G and GO) into new composites with ferroelectric polymers PVDF and P(VDF-TrFE), were performed, both experimentally and using computational molecular modelling [6, 11, 23, 24]. Also, using the same MD run method, pyroelectric coefficients in PVDF and PVDF-G were calculated [24-26]. In this work we consider some complex compositions of this type, consisting of PVDF and G or GO [26-29]. We also give a short review of the models aimed at investigation of their piezo- and pyroelectric properties.

## 2. COMPUTATIONAL AND MODELLING DETAILS

Molecular models for pure PVDF (in ferroelectric β-phase), and for composites of PVDF with graphene PVDF-G and with graphene oxide PVDF-GO, as common ferroelectric systems were developed and investigated [6, 11, 23], using HyperChem tool [22]. Different computational methods, including molecular mechanics (MM, Amber, MM+, BIO CHARM) methods and quantum-chemical semi-empirical method (QM,PM3, ZINDO-1), in restricted Hartree-Fock (RHF) and unrestricted Hartree-Fock (UHF) approximations, were used.The molecular model of the PVDF chain (denoted by PVDF12) was proposed by us earlier in [19] and then was used and developed in [20, 21, 23] to determine the effect of the electric field on the polarization and for calculation of the piezoelectric coefficients, when applying an external electric field E (using the HyperChem software [22]). Figure 1 shows our original model [19] and its central part used in these piezoelectric effects calculations [21, 23].The aim of the usage of both the MM and QM methods used for

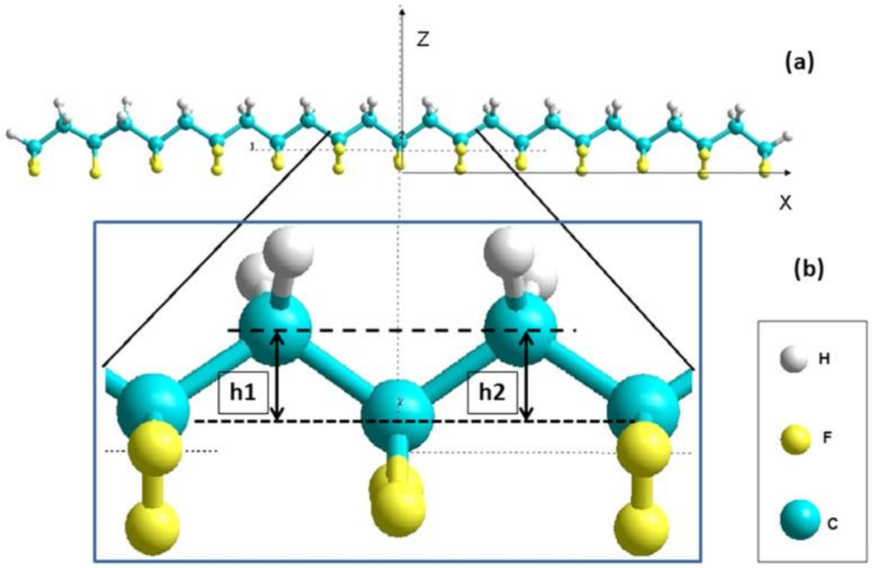

Figure 1. Model of PVDF chain: (a) PVDF with 12.5 units (marked PVDF12) and (b) Its central part.

molecular modeling is to search and to obtain the minimum of total or potential energy surface (PES), of the investigated molecular systems which correspond to optimal atomic configuration of the system. Finding of such optimal geometry of all system investigated is executed using the Polak–Ribere (conjugate gradient method) algorithm, which which is included into the HyperChem package [22]. These various computational methods were used for the detailed debugging, validation and testing of the models. For final current calculations of the optimized models the methods BIO CHARM and PM3 in RHF approximations were used mainly in this work.

Further, the G and GO models were developed and several models of their composites with PVDF were proposed [6, 11, 23]. Such initial models with 96 carbon atoms (Gr96H) in one layer are presented in Figure 2 (a, d), as well as G-layers models with PVDF chain in various configurations in Figure 2 (b, c, d, e, f). For calculation of the piezoelectric coefficients the special algorithm elaborated for thin films in our previous works [ 20-23] was used and now it is applied for fiber models too. These data obtained are presented and analyzed in Sec. 3.1 and 3.3.

For calculation of the pyroelectric coefficients it is necessary to know the temperature dependence of the polarization [1-3]. These data can be obtained by using the MD run approach [20 - 22], which is included in HyperChem tool too. This method was similarly used and developed early, for example, for investigation of the polarization switching time in similar thin ferroelectric films [21], using quantum method PM3. Now we use this MD approach to study the dynamics of polarization change, which take place as the temperature of the studied system rises, which enables us to calculate

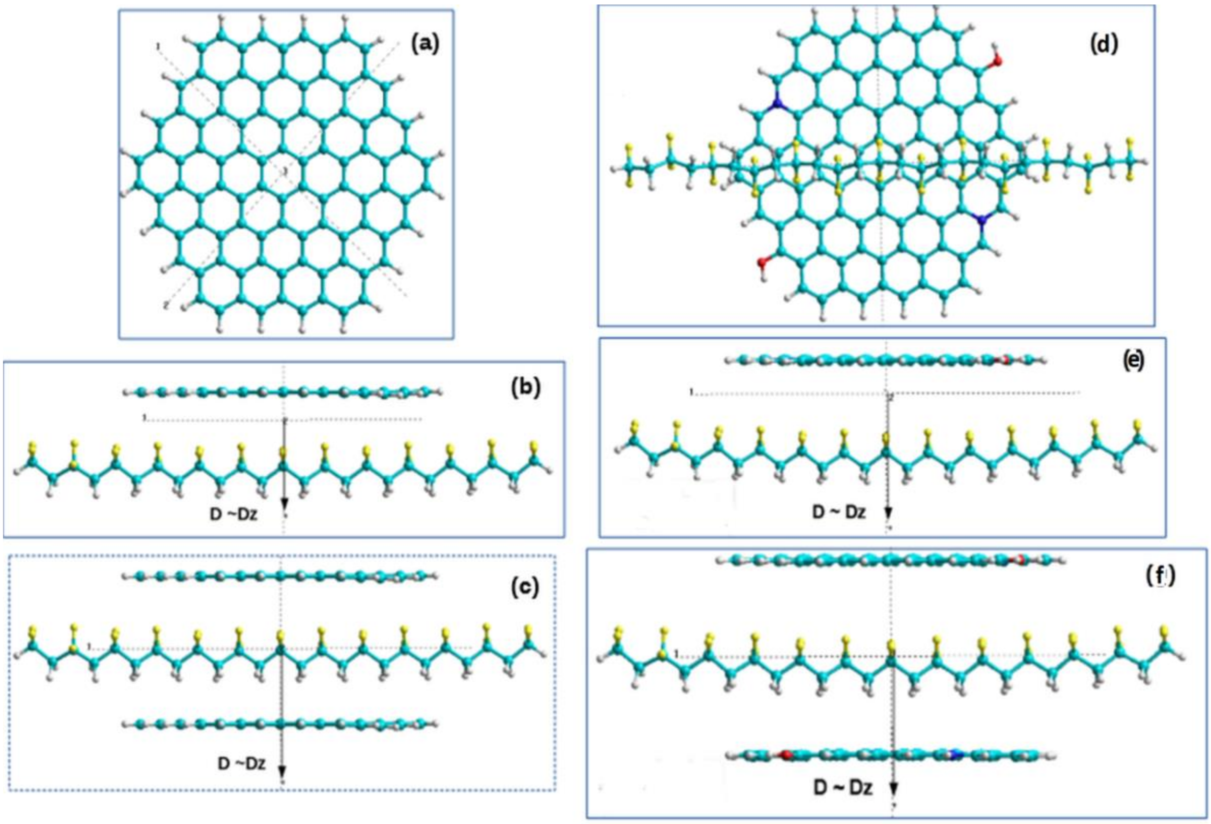

Figure 2. Initial states for several models for the composites of PVDF with G/GO:
(a) initial G layer model from 96 carbon atoms arranged by hydrogen atoms H (Gr96H), in Z view projection, (b) PVDF chain and G layer (PVDF12+Gr96H) in Y view, (c) PVDF and 2 G layers (PVDF12+2Gr96H) in Y view, (d) GO layer (with 2 nitrogen atoms N and 2OH groups) and PVDF chain (PVDF12+Gr96H2N2O2H) in Z view, (e) the same model in Y view, (f) PVDF and 2 GO (PVDF12+2Gr96H2N2O2H).

the pyroelectric coefficients. Such an approach was used to determine pyroelectric coefficients, for example, in our recent work for the PVDF-G composite [24]. In present work, additionally some more complex various model compositions, consisting of PVDF and either G or GO are considered and analysed in Sec. 3.2.

To check these molecular modeling and MD run data in our work [24] was proposed to perform the polarization calculations using the well-known relation from Landau-Ginzburg-Devonshire (LGD) phenomenological theory of the ferroelectrics with the first order phase transition (PT1) [1-3]. From the basic phenomenological theory of ferroelectrics it is known that the values of piezoelectric and pyroelectric coefficients are defined by relations described in [1-3], through the behavior of polarization P depending on temperature T by square root law. This behavior is determined by LGD theory parameters: Curie-Weiss constant *C*, Curie temperature $T_0$, dielectric constant $e_0$, phenomenological coefficients a, b, g and the value of the spontaneous polarization $P_{S0}$ at the phase transition temperature $T=T_c$ for the case $E = 0$. Using such square root formula for PT1 from LGD theory in the dimensionless form with reduced temperature *t* (similarly as [3, 24]), it could be written:

$$P = P(E=0) = \pm P_{S0}\left[\frac{2}{3}\left(1+\sqrt{1-t}\right)\right]^{\frac{1}{2}},$$

$$P_{S0}^2 = -\frac{3}{4}\frac{\beta}{\gamma}, t = 4\alpha\frac{\gamma}{\beta^2}, \alpha = \frac{(T-T_0)}{C\varepsilon_0}, \ T < T_0 \qquad (1)$$

For PVDF known data of the LGD theory coefficients and PT1 parameters [3, 24] lead to the value of $P_{S0} \sim 0.11$ C/m$^2$, that allow us to calculate *P*(*T*) dependence on temperature *T* and therefore pyroelectric coefficients. These data are used and analyzed in Sec. 3.2.

## 2. MAIN RESULTS OBTAINED FROM MOLECULAR MODELLING STUDIES AND DISCUSSION

### 3.1. Piezoelectric coefficients calculations

The mechanism of piezoresponse evolution of the composite was studied using our previous computational molecular models of PVDF chain (Figure 1(a) and (b)). The behavior of piezoelectric response in an electric field and the data on the average piezoelectric coefficients (calculated using algorithm [20, 23]): here **$\langle d_{33}\rangle = (\Delta h_i/U)*$**$\varepsilon$, where **U** is voltage for the applied electric field value and **$\Delta h_i$** is a change of PVDF chain's skeleton height **$h_i$** (i=1, 2 as is shown in Figure 1) which takes place after geometry optimization at each step of calculations for every applied electric field value, $\varepsilon$ is dielectric permittivity ($\varepsilon = 10$).

Additionally, the piezoelectric coefficient calculated with the use of the electromechanical coupling relation: **$d_{33} = 2Q\varepsilon\varepsilon_0 P$** (where **Q** is electrostriction coefficient, **P** is polarization) [20]. The symmetrized models were used both for graphene oxide based on graphene layer consisting of 54 carbon atoms (Gr54) and 96 carbon atoms (Gr96). These graphen oxides contained oxygen, OH groups (marked by Gr96N2O2H2), and COOH groups (marked shortly for simplicity by Gr96NO), surrounded by hydrogen (Gr54H, Gr96H) [6, 11, 23]. In these works several simplest models were developed for PVDF/Graphene oxide complex (Figure 2) and their piezoelectric coefficients were computed by the same calculation algorithms as described in detail [20, 23]. There we started with considering the simplest models of PVDF/Graphene oxide composites in the main three variants: 1) with H-side (hydrogen atom side) connected from PVDF to the graphene oxide, 2) with F-side (fluorine atom side) connected from PVDF to graphene oxide (these both first variants show approximately the same values of piezoelectric coefficients) and 3) Graphene Oxide/PVDF with both sides (sandwich type). The more complex models were considered too. It is interesting that the data obtained depend on the orientation of the GO layer: we compare two different orientations marked as "rot1" and "rot2." Similarly a more complex new multi-layered structure was considered in [27]. This work is developed further. The main calculated results are presented in Table 1.

Experimental results qualitatively correlate with those obtained in the calculations [6, 11, 20, 23, 30]. We can assume that experimental data obtained for the P (VDF-TrFE)-GO composite film at the low GO content can be associated with the model constructed for the case of PVDF with

Table 1. Calculated values of the piezoelectric coefficients $<d_{33}>$ for PVDF-G/GO composites.

| # | Type of the model structures | $<d_{33}>$, pm/V | Experimental $<d_{33}>$, pm/V |
|---|---|---|---|
| 1 | PVDF12/Gr54-H-side | -12.29 | |
| 2 | PVDF12/Gr54-F-side | -12.16 | |
| 3 | PVDF12 / Gr96N2O2H2 | - 14.6 | |
| 4 | PVDF12 /Gr96NO | - 13.5 | |
| 5 | Gr96N2O2-H2 / PVDF12 / Gr96N2O2-H2 | - 29.8 | |
| 6 | Gr96NO /PVDF12/ Gr96NO (rot1)* | -22.8 | |
| 7 | Gr96NO /PVDF12/ Gr96NO (rot2)* | -14.5 | |
| 8 | Gr96NO /PVDF12/ Gr96NO (average rot1&rot2) | -18.7 | |
| 9 | Multi-layered models [27] | -22 | |
| 10 | PVDF12 [20] | -38.5 | -20.0 … -39.0 (cited in [20]) |
| 11 | P(VDF-TrFE) [6] | | -38.0 |
| 12 | P(VDF-TrFE)/GO [6] | | -30.1 |
| 13 | P(VDF-TrFE) [30] | | -25.0 … -55.0 |
| 14 | P(VDF-TrFE)/BPZT [30] | | -18.0 … -40.0 |

graphene oxide from one side only. This leads to a reduction in the piezoresponse coefficient. This effect may be due to the possible effect of shielding from the graphene layer on the charges and the PVDF dipoles. An increase in the GO content most probably corresponds to the model where the availability of sandwich clusters in the composite is implied.

Quality manifestation of the effect of the graphene oxide grains on the piezoelectric properties of the composite films can be observed at the boundaries of graphene grains [6, 11]. That may lead to the formation of alternating layers of graphene oxide and PVDF on the boundary grains. Based on the results of our simulations the piezoresponse for sandwich structures PVDF/GO must be increased (Table 1). This is qualitatively observed from our piezo-response force microscopy (PFM) measurements [6, 11], and demonstrates a possible existence of such effects which take place due to their layered structure. This suggests that in the heterostructures under controlled alternating layers, this effect will be clearer and they can be controlled.

## 3.2. Pyroelectric coefficients determination by molecular dynamics method

Simulation of any system by molecular dynamics (MD) method allows us to obtain the temperature dependence of many physical characteristics for studied systems. The important characteristics for ferroelectrics is the polarization dependence on temperature changes (which is described by a well-known square root low [1-3]). Such simulation of the temperature dependence using special MD option in HyperChem tool [12, 21, 22] was made in

Table 2. Pyroelectric coefficients from MD calculated data [26] and obtained from experiments [25].

| Type of model system or samples | $p$, μC/(m$^2$K) (average by several MD run) | | $V_G/V$, $V_{GO}/V$ | $p$, μC/(m$^2$K), experim. data [25] | |
|---|---|---|---|---|---|
| Pure PVDF12 | 34.1 - 40.8 | | | 39.5 for P(VDF-TrFE) (70:30) | |
| Composites | with G | with GO | | Non-polarized samples with GO | Polarized samples with GO |
| PVDF12+Gr96H | 135.8 | | 0.65 | - | - |
| 2PVDF12+Gr96H | 64.9 | | 0.48 | | |
| PVDF12+2Gr96H | 18.2 | | 0.79 | | |
| 2PVDF12+2Gr96H | 22.9 | | 0.65 | | |
| PVDF12+Gr96H2N2O2H | | 29.2 | 0.65 | 33.3 | 15.0 |
| 2PVDF12+Gr96H2N2O2H | | 57.2 | 0.48 | | |
| 2PVDF12+Gr96H2N2O2H (MM+) | | 48.9 | | | |
| PVDF12+2Gr96H2N2O2H (MM+) | | 27.4 | 0.79 | | |
| 2PVDF12+2Gr96H2N2O2H | | 58.3 | 0.65 | | |

this work. A special set of parameters necessary for MD run are described earlier [24], as well as the MD run calculation algorithm. The semi-empirical quantum method PM3 in RHF approximation was used for all these calculations and for each MD run step. These data allow us to obtain the polarization values for all the systems modelled under all changes of the temperatures and then to calculate the pyroelectric coefficients as **$p = \Delta P/\Delta T$** [1-3, 24]. For each temperature polarization was determined, through optimized dipole moment and volume of the full system, and corresponding value of the pyroelectric coefficient was calculated at each step.

From these data obtained the pyroelectric coefficient for the pure PVDF chain molecular model was calculated: **$p = \Delta P/\Delta T = \sim 34 - 41$** μC/(m$^2$*K), which is in line with many known data for PVDF and copolymers systems [1-3, 13-23] (see Table 2).

To check these data we additionally performed calculations using square-root relation (1) for polarization depending on temperature by Landau-Ginzburg-Devonshire (LGD) theory of the ferroelectrics [3, 24]: these data calculated are comparable with the data obtained by MD run. The MD runs were performed for several complex models [26] (some of which are shown in Figure 2 for the initial states). Corresponding data of the pyroelectric coefficients for all computed models [26] are collected in Table 2. These are important results, which show that G and GO components embedded into composite material lead to observed changes and differences in the pyroelectric coefficients values. This influence depends greatly on the G and GO content: for one G layer model we have a rise of the pyroelectric coefficient (as compared with pure PVDF), while for 2 G layers model (sandwich) value of the pyroelectric coefficient is nearly tenfold lower than in the case of one G layer model. The data obtained show that the values of the pyroelectric coefficients computed by the MD run method proposed are very close to experimental data from [25] as well as for PVDF and P(VDF-TrFE) from many other published data [1-3, 13-18].

### 3.3. Nanofibers composites

Piezoelectricity in macromolecule polymers has been gaining immense attention, particularly for applications in biocompatible, implantable, and flexible electronic devices. This paper [28] describes composite fibers of copolymer poly trifluoroethylene wiz. (P(VDF-TrFE)) with graphene (G) and graphene oxide (GO). Experimental and theoretical investigations were done to understand the effect of the G and GO concentration on polarization behavior of bulk composites and composite fiber microstructures. The electromechanical properties of the PVDF/G and PVDF/GO nanofibers are investigated in terms of piezoresponse mapping, local hysteresis loops, polarization reversal by advanced piezoresponse force microscopy (PFM) and Kelvin Probe Force Microscopy (KFM).

In order to understand the mechanism of piezoresponse evolution of the composite we used the models of PVDF chains, interacting with Graphene/GO layers, the data on its behavior in an electric field and the data computed for piezoelectric coefficients using HyperChem, as described above. But, the new curved models of the PVDF chains as well as the G/GO layers were developed [28] in these cases (see Figure 3 as a simple model case: pure PVDF (a) and with one curved Graphene layer (b)). Experimentally measured results qualitatively correlate with the data obtained in these calculations (Table 3) [28, 29].

An optimization strategy which determines the changes in the atomic configuration of studied clusters [20,23] assumes several steps of models, the first one considers an absence of electric field which allows to find the initial optimal atomic positions of modelled composite structure and to determine the initial optimal parameters of PVDF chain heights in its central part (h1, and h2). The second step of model considers an external electric field Ez with Z orientation (along the main polarization vector of PVDF), this model allows to find out the optimal geometry for new atomic configuration under action of electric field. The third step of model assumes the changes of the main parameters (h1 and h2, Figure 3) from initial optimal parameters, which allows to determine the deformation Dh1 and Dh2, and to calculate the corresponding values of voltage U = Ez*h and, finally, the piezoelectric coefficient $d_{33} = \varepsilon(\Delta h/U)$ was computed, using a dielectric permittivity value of ε = 10 [20, 23]. Comparison with the data known for $d_{33}$ attributed to initial PVDF samples testifies that under the influence of graphene oxide layer the piezoelectric coefficient $d_{33}$ of new composite structure is decreased. It has nearly three times

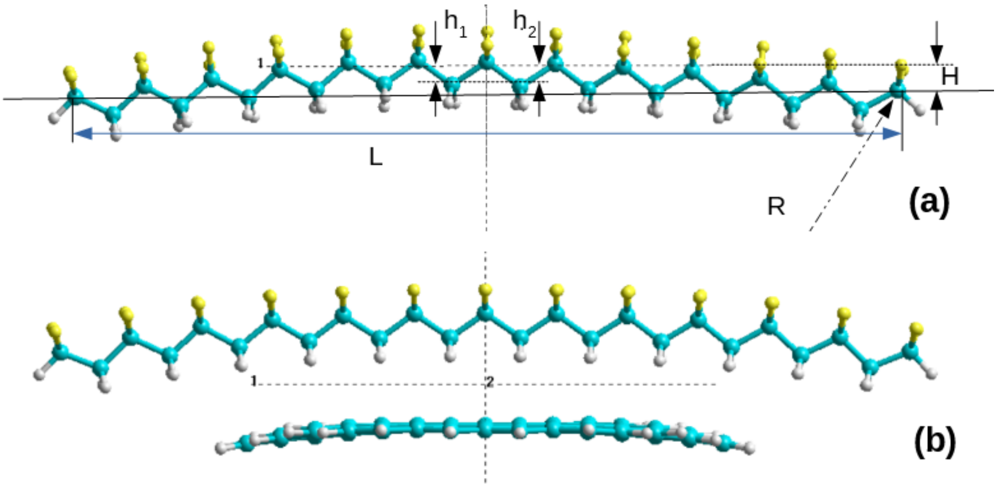

Figure 3. Model of curved PVDF chain (a) and curved composite PVDF-Graphene (b), R - radius of curvature, L - chord of curvature, H - hight of curved chain on length of chord L; $h_1$ and $h_2$ are similar as above in [20, 23].

Table 3. The piezoelectric coefficients $d_{33}$ calculated for different types of structures of Graphene Oxide with OH and COOH groups and PVDF: for flat layer models and for curved fiber models (for comparison data from paper [20, 23] were taken, data present only in absolute values, without its negative sign).

| # | Models Content | Flat models* $d_{33}$, pm/V | Films (experimental) $d_{33}$, a.u., V | Curved models $d_{33}$, pm/V | Fibers (experimental) $d_{33}$, a.u. |
|---|---|---|---|---|---|
| 0 | PVDF pure (chain) | 38.5 | 7.5 | 22.3 | 20.8 |
| 1 | PVDF/G54 1 side | 12.2 | - | - | - |
| 2 | PVDF/G54H 1 side | 9.8 | - | 16.7 | 11.1 |
| 3 | G54H/PVDF/G54H 2 sides (sandwich) | 19.0 | - | 34.8 | 22.7 |
| 4 | G96H/PVDF/G96H 2 sides (sandwich) | - | - | 51.9 | 46.9 |
| 5 | PVDF/GO1 1 side | 14.6 | 5.9 | | |
| 6 | PVDF/GO2 1 side | 13.5 | - | | |
| 7 | GO1/PVDF/GO1 2 sides (sandwich) | 18.7 | 6.7 | | |
| 8 | GO2/PVDF/GO2 2 sides (sandwich) | 29.8 | | | |

***** [20,23 ]

Abbreviations used in Table 3 are the following: GO1 is graphene oxide which contain COOH groups ($Gr96N_2O_2H_2COOH_2$, which was abbreviated as Gr96NO in [23, 28, 31]), GO2 is graphene oxide with OH group written as formula $Gr96HN_2O_2H_2$ above.

lower value: $d_{33}$ = 14.6 pm/V (or pC/N) for the simple flat models (with one side H or F of PVDF chain—Figure 2a), which interacting with one GO layer (with OH groups), as compared with the average value of the pure PVDF $d_{33}$ = 38.5 pm/V (pC/N). It is important to note, that the sign of $d_{33}$ coefficient is negative in all cases as it was established in [22, 23] for the initial pure PVDF, it is caused by specific mechanism of PVDF chain deformation under an applied electric field. In the case of flat with double graphene oxide layers (sandwich model structure) the piezoelectric coefficient $d_{33}$ is increased to the value of $d_{33}$ = ~ 29.8 pm/V (pC/N) (Figure 2b, and see in Table 2, data for flat models).

The experimental results qualitatively correlate with those obtained in the calculations (see Tables 2 and 3). We assume that the experimental data obtained for the composite with small amount of graphene oxide correlate to the model constructed for the PVDF chain interacted with graphene oxide from one side only. The results obtained for this case show a reduction in the piezo-response as well as in the piezoelectric coefficient. From the other side, piezoelectric properties of the composites with larger GO content correspond to the model assuming the sandwich-like clusters in the composite. The experimental data testify a decrease in the piezoelectric signal in these composites which is caused by statistical dispersion and disorientation of graphene oxide layers and PVDF chains (or layers). Uncontrolled thickness of the individual layers of graphene oxide and PVDF component can also affect piezoelectric properties of the composites. Statistical disorder obtained in these cases could not yield an exact match with the simulation performed. However, even at low concentrations, the effect of molecular ordering is observed, and for 20% GO composite the probability of the formation of sandwich structures (as proposed in our modeling) is quite significant. Furthermore, in the case of controlled hetero-structures we can consider a much greater effect and results will be closer to experimental.

The case of model with curved PVDF chain and Graphene layers were considered and discussed here also [6, 26, 27, 29-30]. This situation could be corresponding to the fiber′s surface—it is a curved surface with some radius R. In the experimental case it is approximately ~R ~50...100 nm. But in our modeling, we use approximately R ~10 nm (and more) for most bright and expressive influence of such curvatures, which imitates the curved surface. This radius could be simply determined from usual geometry using formula (see about of some geometrical chord (with high H and length L) determinations on Figure 3a:

$$R = (H^2 + L^2/4)/(2H) \qquad (2)$$

It is known from the literature that for the case of curved (or flexible) polymers such as PVDF and related materials, the piezoelectric coefficients are changed in this case [31, 32]. But all computed data used here for our calculation of $d_{33}$ shown the series of such curved models in this case are similar as in our previous flat models and following results of calculated piezoelectric coefficients are presented in Table 3 (last two columns for curved models).

It should be noted that different types of oxidation (O, OH, COOH etc.) may notably change the functional properties of the composites and appropriate calculations becomes to be quite difficult for conventional computer modelling while these models will be considered in our further works. However, despite on used different units for values of the piezoelectric coefficient, current results clearly show the same trend of changes both for the computed and measured data (see Tables 1, 2).

## 4. CONCLUSIONS

The developed models [19-23] and MD run methods [24] allowed us to calculate the temperature dependence of the polarization and calculate the values of the piezoelectric and pyroelectric coefficients for pure PVDF model and for the composites models of PVDF with Graphene and Graphene oxide layers [26, 27, 28, 30]. The values of the piezo- and pyroelectric coefficients obtained for pure PVDF are in line with many known data, the data computed for composite materials are new and predict complex nonlinear behaviour which may take place if Graphene content changes. In some cases (with one G layer models) it was shown that in proposed and developed composite systems the value of the pyroelectric coefficients could be higher than in the initial matrix of pure PVDF materials, while in other cases (for sandwich G models), it can be lowered as compared with initial pure PVDF. These questions need further deepest studies. These data obtained are new and very important. The data obtained predict the novel features of the behaviour of such new composites system based on graphene and ferroelectric copolymers. It is worth noting that the calculated values of the pyroelectric coefficients for various composites from PVDF with G/GO components are close to the values, which are obtained from pyroelectric currents measurements for similar P(VDF-TrFE)/GO composites samples [25]. But, it must be emphasized that these samples were prepared by crystallization from a solution and this fabrication method is different from highly ordered Langmuir-Blodgett technique. For further studies we must focus on the fabrication of the ultrathin Langmuir-Blodgett PVDF or P(VDF-TrFE) films [3, 15-17, 21, 23] deposited directly onto a G/GO layer, which allow us to obtain a very highly ordered multilayered ferroelectric composites with excellent polarization and piezoresponse, as well as pyroelectric properties. This approach must be the next step on the way of creating such new high-quality composites for multifunctional applications. The models developed here predict the important new features and behaviour of these new graphene-PVDF-based composites systems and exactly show us this new way.

## ACKNOWLEDGMENTS

The authors are thankful to the Russian Foundation for Basic Researches (RFBR grant # 19-01-00519 and # 20-51-53014). Prof. Xiang-Jian Meng expresses his gratitude to the National Natural Science Foundation of China (NNSFC) for grant

# 61574151 and Prof. Hong Shen – for grant # 62011530043.

## REFERENCES

[1] M. E. Lines and A. M. Glass, *Principles and Applications of Ferroelectrics and Related Materials,* Clarendon Press, Oxford (1977).

[2] *Ferroelectric liquid crystals Principles properties and applications,* J. W. Goodby, R. Blinc, N. A. Clark, et al., Editors, Gordon and Breach, Philadelphia (1991).

[3] V. Fridkin and S. Ducharme, *Ferroelectricity at the nanoscale. Basics and applications* Springer, Berlin (2014).

[4] V. S. Bystrov, et al., in *Piezoelectricity and ferroelectricity in biomaterials: from proteins to self-assembled peptide nanotubes Piezoelectric nanomaterials for biomedical applications,* G. Ciofani and A. Menciassi, Editors, pp. 187-211, Springer, Berlin (2012).

[5] V. S. Bystrov, E. Seyedhosseini, S. Kopyl, I. K. Bdikin and A. L. Kholkin, *J. Appl. Phys.,* **116,** 066803 (2014).

[6] M. V. Silibin, V. S. Bystrov, D. V. Karpinsky, et al., *Applied Surface Science,* **421,** Pt. A, 42-51 (2017).

[7] S.-H. Bae, O. Kahya, B. K. Sharma, et al., *ACS Nano.,* **7,** 3130-3138 (2013).

[8] R. Md. Ataur, L. Byung-Chul, P. Duy-Thach and C. Gwiy-Sang, *Smart Mater. Struct.,* **22,** 10-085017 (2013).

[9] T. Kuilla, S. Bhadra, D. Yao, N. H. Kim, S. Bose and L. H. Lee, *Prog. Polym. Sci.,* **35,** 1350-1375 (2010).

[10] X. Wang, P. Wang, J. Wang, W. Hu, X. Zhou, N. Guo, et al., *Adv. Mater.,* **27,** 6575-6581 (2015).

[11] V. S. Bystrov, I. K. Bdikin, M. V. Silibin, D. V. Karpinsky, et al., *Ferroelectrics,* **509,** 124-142 (2017).

[12] E. V. Paramonova, S. V. Filippov, V. E. Gevorkyan, L. A. Avakyan, X. J. Meng, B. B. Tian, et al., *Ferroelectrics,* **509,** 143-157 (2017).

[13] L. Blinov, V. Fridkin, S. Palto, A. Bune, P. Dowben and S. Ducharme, *Uspekhi Fizicheskikh Nauk,,* **170,** 247-262 (2000).

[14] A. V. Bune, V. M. Fridkin, S. Ducharme, et al., *Nature,* **391,** 874-877(1998).

[15] H. Qu, W. Yao, J. Zhang, S. Dusharme, P. A. Dowben, A. V. Sorokin and V. M. Fridkin, *Appl Phys. Lett.,* **82,** 4322-4324 (2003).

[16] H. Kliem and R. Tardos-Morgane, *J. Phys.: D Appl. Phys.,* **38,** 1860-1868 (2005).

[17] V. S. Bystrov, I. K. Bdikin, D. A. Kiselev, S.G. Yudin, V. M. Fridkin and A. L. Kholkin, *J Phys.: D Appl. Phys.,* **40,** 4571-4577 (2007).

[18] R. V. Gaynutdinov, S. Yudin, S. Ducharme and V. Fridkin, *J. Phys.: Condens. Matter,* **24,** 015902 (2012).

[19] V. S. Bystrov, N. K. Bystrova, E. V. Paramonova, et al., *J. Phys.: Condens. Matter,* **9,** 456210 (2007).

[20] V. S. Bystrov, E. V. Paramonova, I. K. Bdikin, et al., *J. Mol. Model.,* **19,** 3591-3602 (2013).

[21] V. S. Bystrov, *Physica B,* **432,** 21-25 (2014).

[22] *Hypercube Inc and HyperChem* (versions 7.51 and 8.0), Hypercube Inc., Gainesville (2002).

[23] V. S. Bystrov, I. K. Bdikin, M. Silibin, et al., *J. Mol. Mod.,* **23,** 128 (2017).

[24] V. S. Bystrov, I. K. Bdikin, M. Silibin, X. J. Meng, et al., *J. Phys. Conf. Series,* **1053,** 012043 (2018).

[25] M. Wojtas, D. V. Karpinsky, M. V. Silibin, et al., *Polym. Test.,* **60,** 326-332 (2017).

[26] V. S. Bystrov, I. K. Bdikin, M. V. Silibin, X. J. Meng, T. Lin, et al., *Ferroelectrics,* **541,** 17-24 (2019).

[27] V. S. Bystrov, I. K. Bdikin and M. V. Silibin, Ferroelectric Polymers PVDF and P(VDF-TrFE) Films and Their Composites With Either Graphene or Graphene Oxide Molecular Modeling and Experimental Observations, In: Saleem Hashmi (editor-in-chief), *Reference Module in Materials Science and Materials Engineering* Oxford Elsevier 2018 pp. 1-11 (2018).

[28] M. V. Silibin, V. S. Bystrov, D. A. Kiselev, et al., Local piezoelectric properties of P(VDF-TrFE)/Graphene and P(VDF-TrFE)/Graphene oxide composite fibers, in *International Conference on Nanomaterials Science and Mechanical Engineering* (University of Aveiro Portugal July 16-18 2018) Book of Abstracts, Editors: Igor Bdikin, Victor Fernando Santos Neto, ISBN 978-972-789-547-2, Aveiro: UA Editora, Universidade de Aveiro, 2018, 95 pages, p. 66 (2018).

[29] J. Belovickis, M. Ivanov, S. Svirskas, et al., *Phys Stat Sol (b),* **254,** 1700196 (2017).

[30] M. Silibin, D. Karpinsky, V. Bystrov, et. al., *C – J. of carbon researches,* **5,** 48 (2019).

[31] G. Li, E. Furman, G. H. Haertling, *J. Am. Ceram. Soc.* **80**, 1382-1388 (1997).

[32] L.-H. Kang, J.-H. Han, *Smart Mater. Struct.,* **19**, 94006 (2010).

**NANOMATERIALS**
**SCIENCE & ENGINEERING**
Vol. 2, No. 2, pp. 93-98 (2020)

RESEARCH ARTICLE

https://doi.org/10.34624/nmse.v2i2.15737

# Crystal structure and magnetic properties of (1-x)BiFeO3 – xBaTiO3 ceramics across the phase boundary

**D.V. Zhaludkevich[1*], S.I. Latushka[1], T.V. Latushka[2], A.V. Sysa[3,4], Yu.P. Shaman[3,4], D.A. Dronova[3], A.N. Chobot[1], G.M. Chobot[5], K.N. Nekludov[3], M.V. Silibin[1,3,4,6], D.V. Karpinsky[1,3]**

[1] *Scientific-Practical Materials Research Centre of NAS of Belarus, 220072 Minsk, Belarus*
[2] *Belarusian State Medical University, 220116 Minsk, Belarus*
[3] *National Research University of Electronic Technology "MIET", 124498 Zelenograd, Moscow, Russia*
[4]*Scientific-Manufacturing Complex "Technological Centre", 124498 Zelenograd, Moscow, Russia*
[5] *Belarusian State Agrarian Technical University 220023 Minsk, Belarus*
[6] *Institute for Bionic Technologies and Engineering, I.M. Sechenov First Moscow State Medical University, 119991 Moscow, Russia*

**Corresponding author, e-mail address: jeludkevichdima@gmail.com*

Received 7 May 2020; accepted 21 May 2020; published online 10 June 2020

## ABSTRACT

The crystal structure and magnetic properties of lead-free ceramics (1-x)BiFeO$_3$ - xBaTiO$_3$ ($x < 0.40$) prepared by solid state reaction method were studied depending on the chemical composition and temperature. An increase in the concentration of barium and titanium ions leads to the structural transition from the polar rhombohedral structure to the cubic structure through the phase coexistence region characterized by a formation of pseudocubic phase. The isothermal magnetization measurements indicate nearly linear field dependences of magnetization in the temperature range 5 - 300 K which corresponds to a dominance of antiferromagnetic structure in the compounds with $x < 0.3$. Negligible value of remnant magnetization observed for the compounds having dominant rhombohedral structure diminishes in the compounds with (pseudo) cubic structure. The correlation between the type of structural distortion and magnetic structure is discussed based on the neutron and X-ray diffraction data as well as the magnetization measurements.

## 1. INTRODUCTION

Materials based on bismuth ferrite attract great attention of the scientific community due to wide variety of structural and magnetic phase transitions [1-10]. While solid solutions based on bismuth ferrite have significant disadvantages - low residual magnetization, high conductivity, small magnitude of magnetoelectric interaction, which significantly limit the scope of their possible applications [8,11-14]. Some of these disadvantages can be overcome using various chemical doping schemes. Thus, chemical substitution of bismuth ions by alkaline-earth elements and substitution of iron ions by other transition metals elements can be used as an effective tool for controlled changes of crystal structure and functional properties [14-19]. The use of alkaline earth ions as dopant ions leads to a significant change in the crystal structure of the compounds, thus the substitution of Ba$^{2+}$ ions having ionic radius larger than that of Bi$^{3+}$ ions causes a stabilization of cubic structure through an intermediate phases [1, 3, 20, 21].

Simultaneous substitution of perovskite lattice in A- and B- positions using alkaline earth ions and transition metals respectively allows to control the crystal structure of the compounds and to modify their magnetic properties. It is also possible to control the conductivity of the $BiFeO_3$ based compounds and oxygen stoichiometry associated with transport properties [22]. It is known that chemical substitution by barium ions with ions having large ionic radius increases the concentration region of structural stability of the polar rhombohedral phase, and the substitution of iron ions by titanium ions allows to control magnetic properties of the compounds [22, 23].

The present work is focused on the correlation between the crystal structure and magnetic properties of the compounds across the phase transition from the rhombohedral phase to the cubic phase. It is shown that utilizing the mentioned chemical doping scheme allowed to control both electric dipole and magnetic orders in the solid solutions $(1-x)BiFeO_3$ - $xBaTiO_3$, which makes them promising materials to be used in the field of information and energy-saving technologies. The functional materials based on $BiFeO_3$ can be also used as magnetic sensors, capacitive electromagnets, magnetic memory elements, microwave filters and other devices which do not require constant electric currents and associated heat loss.

## 2. EXPERIMENTAL

Ceramic samples of $Bi_{(1-x)}Ba_xFe_{(1-x)}Ti_xO_3$ system with concentrations of the dopant ions in the range 0.15 ≤ x ≤ 0.40 were prepared by the solid-state reaction method [3,18]. High-purity oxides $Bi_2O_3$, $Fe_2O_3$, $TiO_2$ and carbonite $BaCO_3$ (Sigma-Aldrich, ≥ 99%) taken in stoichiometric ratio were mixed using planetary ball mill (Retsch PM 200). The samples were uniaxially pressed into tablets with a diameter of 10 mm. Preliminary synthesis was performed at 900 °C, after intermittent grinding the samples were finally synthesized at temperatures 910 - 945°C (synthesis temperature was gradually increased with the dopants concentration) [22, 24]. After synthesis the samples were cooled down to room temperature with a cooling rate of 100 °C/h.

X-ray diffraction patterns were recorded in the 2thetta range of 20 - 80° with a step of 0.02° using Bruker D8 Advance and Rigaku D/MAX-B diffractometers with Cu-Kα radiation. Neutron powder diffraction (NPD) measurements were performed using high-resolution neutron powder diffractometer FIREPOD (λ=1.7977Å, E9 instrument, HZB). The diffraction data were analyzed by the Rietveld method using the FullProf software [25]. Magnetization measurements were performed in magnetic fields up to 14 T using physical properties measurement system from Cryogenic Ltd.

## 3. RESULTS AND DISCUSSIONS

The refinement of the diffraction data obtained for the compounds of the system

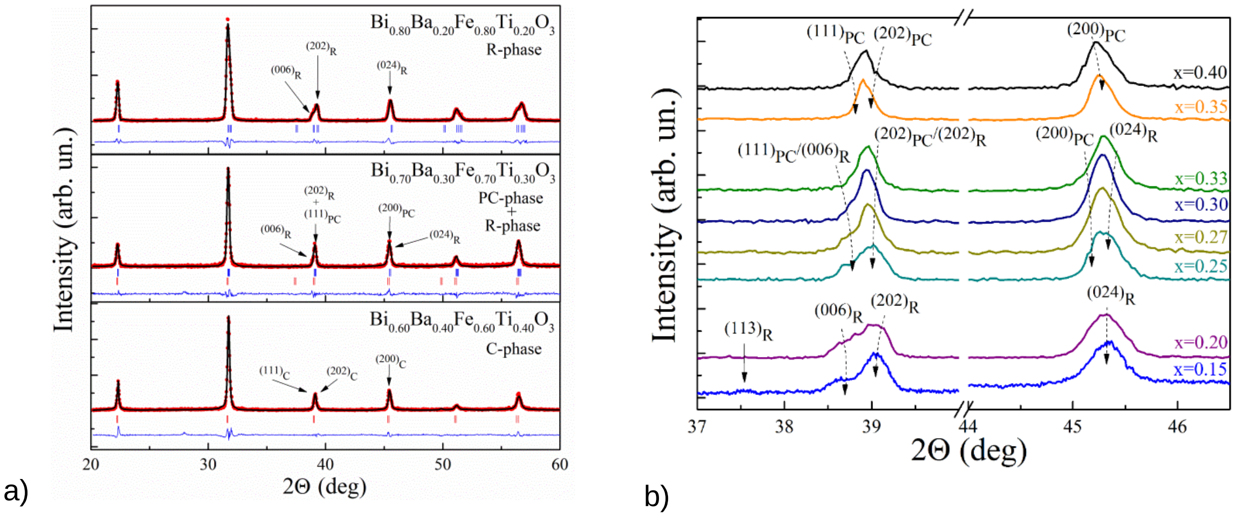

Figure 1. (a) Room-temperature XRD patterns of the compounds $Bi_{(1-x)}Ba_xFe_{(1-x)}Ti_xO_3$ x= 0.20; 0.30; 0.40; observed and calculated profiles are marked by dots and solid line respectively, the line below the pattern refers to the difference between the profiles. The upper row of the ticks denotes Bragg reflections ascribed to the rhombohedral phase, the second row – to the cubic phase; (b) the evolution of the selected diffraction peaks depending on the concentration.

$Bi_{(1-x)}Ba_xFe_{(1-x)}Ti_xO_3$ has allowed to clarify the evolution of the crystal structure as a function of the dopant concentration and temperature. According to the results of the diffraction measurements, the compounds with $x \leq 0.2$ are characterized by a single-phase rhombohedral structure (Fig. 1a,b). An increase in the concentration of the dopant content leads to a reduction of the rhombohedral distortion, and the structure of the compounds with $x = 0.25 - 0.33$ can be refined assuming a coexistence of the rhombohedral and pseudocubic phases. It should be noted that the pseudocubic phase is observed in the compounds $0.25 < x < 0.40$. This model is in accordance with the results obtained by X-ray and neutron diffraction measurements.

Chemical substitution causes gradual decrease in rhombohedral distortions, which can be estimated by an evolution of the reflection $(113)_R$ (Fig. 1b) associated with a distortion of oxygen octahedra in the *ab* plane of the rhombohedral lattice. The intensity of the reflection gradually decreases with the concentration *x* and disappears for the compound $x = 0.2$. The splitting of the reflections $(202)_R$ and $(006)_R$ ($2\Theta = 39$ °) characterizing rhombohedral distortion gradually decreases with increasing in the concentration of the dopant ions, which indicates gradual decrease in the elongation of the rhombohedral lattice. This splitting completely disappears for the compound with $x = 0.35$, which also confirms the absence of the rhombohedral phase in the compounds with $x > 0.35$. Further substitution leads to a transformation of the crystal structure and the structural state becomes to be single phase with cubic symmetry.

Thus, an increase in the concentration of Ba and Ti ions in the compounds $Bi_{(1-x)}Ba_xFe_{(1-x)}Ti_xO_3$ leads to the structural transition from the polar rhombohedral phase to the cubic phase through the formation of an intermediate pseudocubic phase. Chemical substitution leads to an increase in the unit cell volume which is caused by larger ionic radii of the dopant ions as compared to the radii of Bi and Fe ions [26], wherein the *a*- and *c*-parameters of the unit cell change in different ways (Fig. 2). An increase in the unit cell volume is accompanied by a gradual decrease in rhombohedral distortion, and the angle $\alpha_R$, which describes the rhombohedral distortion, gradually increases from 59.55° for the compound with $x = 0.2$ to 59.98° for the compound with $x = 0.35$, the volume fraction the rhombohedral phase in the last compound becomes to be negligible (Fig. 2).

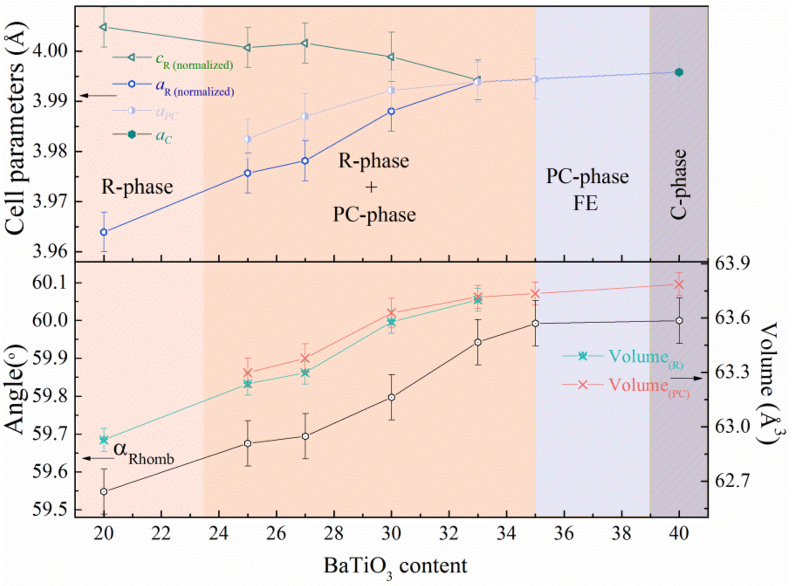

Figure 2. The dopant concentration driven evolution of the unit cell parameters (upper panel), unit cell volume of the rhombohedral and (pseudo)cubic phases and angle $\alpha_R$ calculated for the compounds with $0.2 \leq x \leq 0.4$.

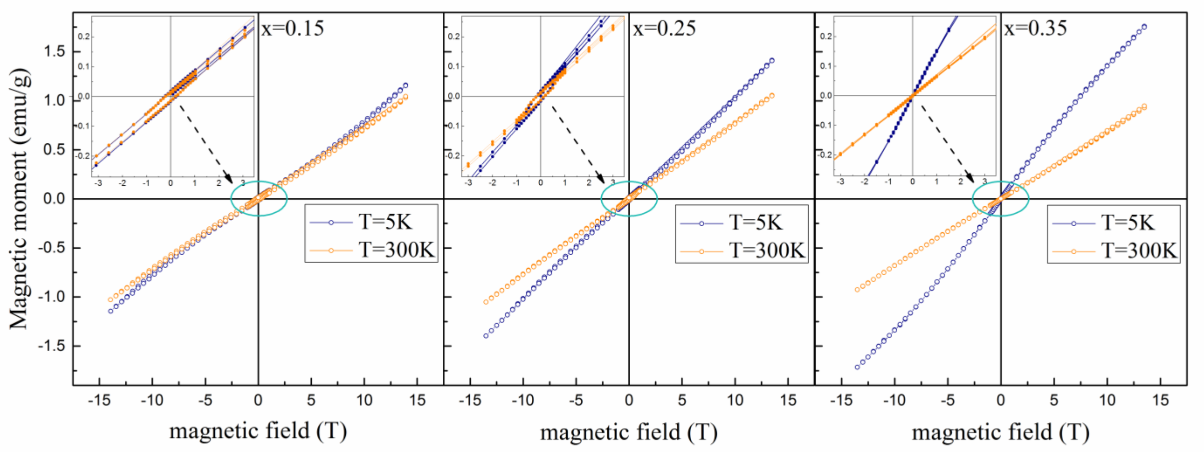

Figure 3. Field dependences of magnetization obtained for $Bi_{(1-x)}Ba_xFe_{(1-x)}Ti_xO_3$ compounds $0.15 \le x \le 0.40$ at temperatures T = 5 K and 300 K. The insets show magnified parts of the magnetization curves near the origin.

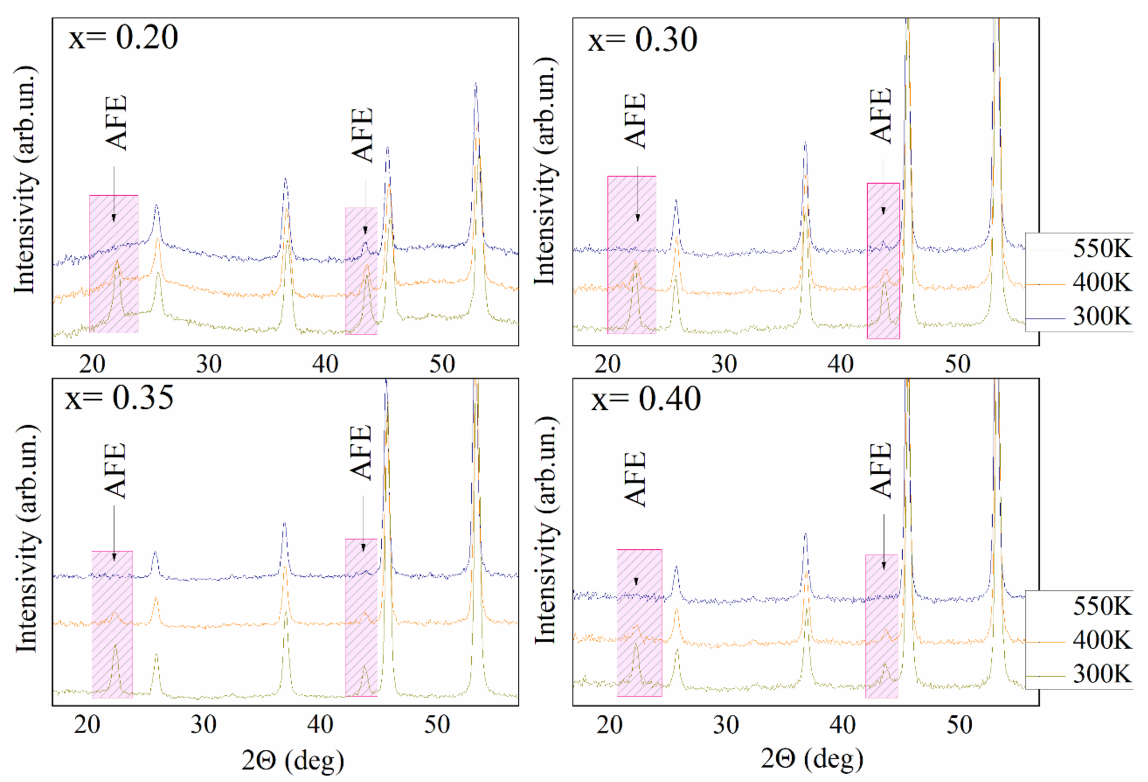

Figure 4. Temperature evolution of characteristic diffraction peaks obtained by neutron diffraction for the compounds $Bi_{1-x}Ba_xFe_{1-x}Ti_xO_3$ with $0.20 \le x \le 0.40$. The diffraction reflections ascribed to magnetic scattering are marked and highlighted by dashed areas.

It should also be noted that the parameter *a*- gradually increases with the dopant content up to x = 0.40, while *c* - parameter begins to significantly decrease only in the compounds with x = 0.27. It should be noted that the *c* / *a* ratio which denotes polar distortion of the lattice decreases down to unity in the compound with x = 0.33.

Magnetization measurements have allowed to reveal a close correlation between the crystal structure and magnetic properties of the compounds. The M(H) dependence obtained for the compound with x = 0.15 has a residual magnetization of about 0.011 emu/g (Fig. 3, inset) and has slightly non-linear character distinctly observed at low temperature which points at a disruption of spatially modulated spin structure at high magnetic fields. The M(H) dependences obtained for compounds with the dopant content x > 0.15 are characterized by nearly linear character of magnetization denoting dominant antiferromagnetic structure. At x = 0.25, the compound is characterized by a mixture of dominant rhombohedral phase and minor pseudo-cubic phase and the remanent magnetization is still present with a value of about 0.014 emu/g. Increase in the concentration of the dopant ions up to x = 0.30 leads to a complete collapse of remanent magnetization which is valid for the compounds with x ≤ 0.4. Such evolution of magnetization is caused by a change in symmetry of the crystal structure from the rhombohedral to the (pseudo)cubic phase. Magnetization data obtained at room temperature indicate the stability of the antiferromagnetic structure in the studied temperature range and the data are in good agreement with the results obtained by the neutron diffraction measurements.

The results of the magnetization measurements performed for the compounds $Bi_{(1-x)}Ba_xFe_{(1-x)}Ti_xO_3$ indicate predominantly antiferromagnetic character of the magnetic structure, which is confirmed by the results of neutron diffraction measurements which indicate the G-type antiferromagnetic structure. Analyzing the data of the neutron diffraction measurements (Fig. 4), it can be stated that the G-type antiferromagnetic structure is stable in the compounds with 0.15 ≤ x ≤ 0.4 in the temperature range 5 K ≤ T ≤ $T_N$. At temperatures above room temperature the diffraction peaks attributed to magnetic scattering become to decrease rapidly till they disappear completely at $T_N$ ~ 500 K for the compounds with x = 0.25 – 0.30. Increase in the dopant concentration up to x= 0.40 leads a reduction of the magnetic transition temperature down to $T_N$ ~ 450 K.

Neutron diffraction data points at G-type antiferromagnetic structure which is stable in the compounds $Bi_{(1-x)}Ba_xFe_{(1-x)}Ti_xO_3$ x ≤ 0.40. The magnetic moment calculated per iron ion of the compound with x = 0.15 at room temperature is about 4.5 $\mu_B$ which is only a bit lower than “spin only” value of the magnetic moment estimated for the iron ions being in 3+ oxidative state ($t_{2g}^5$). The nearly collinear antiferromagnetic structure remains in the compounds upon increase in the dopant content while the magnetic moment associated with the iron ions gradually decreases with x. The compound with the dopant content x=0.25 is characterized by the magnetic moment of ~ 4.2 $\mu_B$, for the compound with x = 0.35 the calculated value of the magnetic moment is ~ 2.9 $\mu_B$. The obtained results are in accordance with the model of diamagnetic dilution of the magnetically active sublattice formed by the iron ions being in 3+ oxidative state, while non-magnetic titanium ions are characterized by the oxidative state of 4+. It should be noted that the remanent magnetization observed in the compounds having dominant rhombohedral phase diminishes in the compounds having dominant (pseudo) cubic phase. This observation is in accordance with the symmetry restrictions, as antisymmetric exchange interactions leading to nonzero remanent magnetization in the compounds with rhombohedral structure are forbidden in the compounds having cubic phase [27-29].

## 4. CONCLUSIONS

The results of diffraction measurements indicate that the single-phase rhombohedral structure is stable in the compounds up to x = 0.2. An increase in the concentration of the dopant content leads to a gradual reduction of the rhombohedral distortion, the structure of the compounds with x = 0.25 - 0.33 can be refined assuming a coexistence of the rhombohedral and pseudocubic phases, further increase in the dopant content leads to the phase transition to single phase cubic structure. Analysis of the isothermal dependences of the magnetization as well as neutron diffraction measurements points at G-type antiferromagnetic structure which is stable in the compounds with 0.15 ≤ x ≤ 0.4 in the wide temperature range in spite of magnetic dilution caused by Ti ions residing in the B-site of perovskite lattice. The obtained results point at strong correlation between the presence of remanent magnetization and structural state of the compounds, thus confirming weak ferromagnetism specific for the compounds having rhombohedral structure; the absence of remanent magnetization in the compounds having (pseudo) cubic structure is in accordance with symmetry restrictions.

## ACKNOWLEDGMENTS

This work was supported by the Russian Science Foundation (project 18-19-00307). The authors acknowledge HZB for the allocation of neutron radiation beamtime and HZB staff for the assistance with neutron diffraction experiments. M.S. acknowledges Russian academic excellence project “5-100” for Sechenov University.

## REFERENCES

[1] S. Kim, G.P. Khanal, H.-W. Nam, I. Fujii, S. Ueno, C. Moriyoshi, Y. Kuroiwa, S. Wada, *J. Appl. Phys.* **122,** 164105 (2017).
[2] R. Haumont, I.A. Kornev, S. Lisenkov, L. Bellaiche, J. Kreisel, B. Dkhil, *Phys. Rev. B* **78,** 134108 (2008).
[3] D.V. Karpinsky, I.O. Troyanchuk, M. Tovar, V. Sikolenko, V. Efimov, E. Efimova, V. Ya Shur, A.L. Kholkin, *J. Am. Ceram. Soc.* **97,** 2631-2638 (2014).
[4] D. Wang, G. Wang, S. Murakami, Z. Fan, A. Feteira, D. Zhou, S. Sun, Q. Zhao, I.M. Reaney, *J. Adv. Dielectr.* **08,** 1830004 (35p) (2018).
[5] D.C. Arnold, K.S. Knight, G. Catalan, S.A.T. Redfern, J.F. Scott, P. Lightfoot, F.D. Morrison, *Adv. Funct. Mater.* **20,** 2116-2123 (2010).
[6] A. Kirsch, M.M. Murshed, M.J. Kirkham, A. Huq, F.J. Litterst, T.M. Gesing, *J. Phys. Chem. C* **122,** 28280-28291 (2018).
[7] D. Wang, A. Khesro, S. Murakami, A. Feteira, Q. Zhao, I.M. Reaney, *J. Eur. Ceram. Soc.* **37,** 1857-1860 (2017).
[8] G. Catalan, J.F. Scott, *Adv. Mater.* **21,** 2463-2485 (2009).
[9] S.M. Selbach, T. Tybell, M.-A. Einarsrud, T. Grande, *Adv. Mater.* **20**, 3692-3696 (2008).
[10] D.V. Karpinsky, I.O. Troyanchuk, O.S. Mantytskaya, V.A. Khomchenko, A.L. Kholkin, *Solid State Commun.* **151,** 1686-1689 (2011).
[11] I.O. Troyanchuk, D.V. Karpinsky, M.V. Bushinsky, V.A. Khomchenko, G.N. Kakazei, J.P. Araujo, M. Tovar, V. Sikolenko, V. Efimov, A.L. Kholkin, *Phys. Rev. B* **83**, 054 109 (2011).
[12] G. Le Bras, P. Bonville, D. Colson, A. Forget, N. Genand- Riondet, R. Tourbot. *Physica B* **406**, 1492-1495 (2011).
[13] I. Levin, M.G. Tucker, H. Wu, V. Provenzano, C.L. Dennis, S. Karimi, T. Comyn, T. Stevenson, R.I. Smith, I.M. Reaney. *Chem. Mater.* **23**, 2166-2175 (2011).
[14] D. Kan, L. Palova, V. Anbusathaiah, C.J. Cheng, S. Fujino, V. Nagarajan, K.M. Rabe, I. Takeuchi. *Adv. Funct. Mater.* **20**, 1108-1115 (2010).
[15] D. Arnold, *IEEE Trans. Ultrason. Ferroelectr. Freq. Control* **62,** 62-82 (2015).
[16] D.V. Karpinsky, I.O. Troyanchuk, N.V. Pushkarev, A. Dziaugys, V. Sikolenko, V. Efimov, A.L. Kholkin, *J. Alloy. Comp.* **638,** 429434 (2015).
[17] V.A. Khomchenko, M.S. Ivanov, D.V. Karpinsky, J.A. Paixao, *J. Appl. Phys.* **122,** 124103 (2017).
[18] D.V. Karpinsky, M.V. Silibin, A.V. Trukhanov, A.L. Zhaludkevich, T. Maniecki, W. Maniukiewicz, V. Sikolenko, J.A. Paixao, V.A. Khomchenko, *J. Phys. Chem. Solids* **126,** 164-169 (2019).
[19] L.H. Yin, W.H. Song, X.L. Jiao, W.B. Wu, X.B. Zhu, Z.R. Yang, J.M. Dai, R.L. Zhang, Y.P. Sun, *J. Phys. D Appl. Phys.* **42,** 205402 (2009).
[20] A. Singh, C. Moriyoshi, Y. Kuroiwa, D. Pandey, *Phys. Rev. B* **88,** 024113 (2013).
[21] I. Calisir, A.A. Amirov, A.K. Kleppe, D.A. Hall, *J. Mater. Chem. A* **6,** 5378-5397 (2018).
[22] D.V. Karpinsky, M.V. Silibin, A.V. Trukhanov, A.L. Zhaludkevich, S.I. Latushka, D. V. Zhaludkevich, V. Sikolenko, V.A. Khomchenko, *J. Alloy. Comp.* **803,** 1136-1140 (2019).
[23] V.A. Khomchenko, D.V. Karpinsky, D.V. Zhaludkevich, S.I. Latushka et. al., *Mater. Lett.* **254,** 305 (2019).
[24] Y.P. Wang, L. Zhou, M.F. Zhang, X.Y. Chen, J.-M. Liu, Z.G. Liu, *Appl. Phys. Lett.* **84,**) 1731 (2004.
[25] J. Rodríguez-Carvajal, *Physica B* **192,** 55-69 (1993).
[26] R. D. Shannon, *Acta. Cryst.* **A32,** 751-767 (1976).
[27] I. Dzyaloshinsky, *J. Phys. Chem. Solids* **4**, 241-255 (1958).
[28] T. Moriya, *Phys. Rev. Lett.* **4**, 228 (1960).
[29] T. Moriya, *Phys. Rev.* **120**, 91 (1960).

**Nanomaterials Science & Engineering (NMS&E), Vol.2, No.2, 2020**

**Department of Mechanical Engineering**
**University of Aveiro**
**Aveiro 3810-193**
**Portugal**

**https://proa.ua.pt/index.php/nmse/**

**ISSN:  2184-7002**

university of aveiro tema centre for mechanical technology and automation